

Unsupervised Machine Learning for Classifying CHIME Fast Radio Bursts and Investigating Empirical Relations

DA-CHUN QIANG,^{1,*} JIE ZHENG,¹ ZHI-QIANG YOU,¹ AND SHENG YANG^{1,2,†}

¹*Institute for Gravitational Wave Astronomy, Henan Academy of Sciences, Zhengzhou 450046, Henan, China*

²*INAF Osservatorio Astronomico di Padova, Vicolo dell’Osservatorio 5, I-35122 Padova, Italy*

ABSTRACT

Fast Radio Bursts (FRBs) are highly energetic millisecond-duration astrophysical phenomena typically categorized as repeaters or non-repeaters. However, observational limitations may result in misclassifications, potentially leading to a higher proportion of repeaters than currently identified. In this study, we leverage unsupervised machine learning techniques to classify FRBs using data from the CHIME/FRB catalogs, including both the first catalog and a recent repeater catalog. By employing Uniform Manifold Approximation and Projection (UMAP) for dimensionality reduction and clustering algorithms (k-means and Hierarchical Density-Based Spatial Clustering of Applications with Noise [HDBSCAN]), we successfully segregate repeaters and non-repeaters into distinct clusters, identifying over 100 potential repeater candidates. Our analysis reveals several empirical relations within the clusters, including the $\log \Delta t_{sc} - \log \Delta t_{rw}$, $\log \Delta t_{sc} - \log T_B$, and $r - \gamma$ correlations, where Δt_{sc} , Δt_{rw} , T_B , r , γ represent scattering time, rest-frame width, brightness temperature, spectral running, and spectral index, respectively. The Chow test results reveal that while some repeaters and non-repeaters share similar empirical relationships, the overall distinctions between the two groups remain significant, reinforcing the classification of FRBs into repeaters and non-repeaters. These findings provide new insights into the physical properties and emission mechanisms of FRBs. This study demonstrates the effectiveness of unsupervised learning in classifying FRBs and identifying potential repeaters, paving the way for more precise investigations into their origins and applications in cosmology. Future improvements in observational data and machine learning methodologies are expected to further enhance our understanding of FRBs.

1. INTRODUCTION

Fast Radio Bursts (FRBs) are highly energetic astronomical phenomena characterized by millisecond-duration emissions. The first FRB signal was discovered in 2007 by Lorimer et al. (2007), and their existence was firmly established in 2013 when Thornton et al. (2013) published observations of four similar events detected by the Australian Parkes Radio Telescope. Since then, FRBs have drawn significant attention in both astronomy and cosmology (e.g., Lorimer 2018; Keane 2018; Petroff et al. 2022; Xiao et al. 2021; Xiao & Dai 2022; Xiao et al. 2022; Zhang 2014; Zhang & Li 2018; Zhang et al. 2021; Zhang & Zhang 2022; Wang et al. 2020a,b; Wang & Zhang 2019; Wang & Wei 2023; Gao et al. 2014; Qiang & Wei 2020, 2021). However, the origin of FRBs remains unknown.

To explore their origin, numerous radio telescopes have dedicated time and efforts on FRBs, such as, the Deep Synoptic Array (DSA; Kocz et al. 2019; Hallinan et al. 2019), Arecibo (Spitler et al. 2014), Parkes (e.g., Lorimer et al. 2007; Burke-Spolaor & Bannister 2014; Petroff et al. 2015; Ravi & Lasky 2014), the Canadian Hydrogen Intensity Mapping Experiment (CHIME; CHIME/FRB Collaboration et al. 2018), the Five-hundred-meter Aperture Spherical Radio Telescope (FAST; Li & Pan 2016), and the Australian Square Kilometer Array Pathfinder (ASKAP; Shannon et al. 2024). So far, nearly a thousand FRBs have been observed (Petroff et al. 2016; CHIME/FRB Collaboration et al. 2021; Jankowski et al. 2023; Xu et al. 2023), with nearly 100 of them have known redshifts (e.g. Law et al. 2024; Sharma et al. 2024; Bhardwaj et al. 2024; Gordon et al. 2023). To date, the largest FRB sample is the first CHIME/FRB catalog (CHIME/FRB Collaboration et al. 2021).

* e-mail: dcqiang@hnas.ac.cn

† Corresponding author; e-mail: sheng.yang@hnas.ac.cn

Based on the observational characteristics, FRBs are broadly classified into two categories, i.e., repeaters and non-repeaters. As the names suggest, repeaters are sources that have exhibited multiple bursts, whereas non-repeaters have only been observed to burst once. Since the discovery of the first repeater, FRB 20121102 (Spitler et al. 2016), more than 50 FRBs have been identified as repeaters to date (CHIME/FRB Collaboration et al. 2021, 2023; Kumar et al. 2019; Kirsten et al. 2022; Fonseca et al. 2020; Niu et al. 2022; Xu et al. 2022), while most of the remaining ones are classified as non-repeaters. However, Ravi (2019) suggests that the volumetric rate of non-repeating FRBs might exceed that of cataclysmic events and the formation rate of compact objects, implying that the majority of FRBs should be repeaters. Some studies also propose that more than half of the FRBs in the first CHIME/FRB catalog could be repeaters (Yamasaki et al. 2023; McGregor & Lorimer 2024). Furthermore, several FRBs initially identified as non-repeaters were later observed to repeat (CHIME/FRB Collaboration et al. 2023). These suggest that many of the FRBs currently classified as non-repeaters might actually be potential repeaters, with only a single burst detected due to various observational factors. As a result, some studies have attempted to identify potential repeaters among apparent non-repeating FRBs, and one of the methods being employed is machine learning.

Machine learning is an artificial intelligence technique that allows computers to learn from data and make predictions or decisions without being explicitly programmed (Cover & Hart 1967; Rumelhart et al. 1986). Machine learning is generally categorized into three types, i.e., supervised learning, unsupervised learning, and semi-supervised learning (e.g. Dempster et al. 2018; Breiman 2001; Chang & Lin 2011; Vapnik 1999). Using algorithms to uncover patterns in the data can be applied to tasks such as classification, regression, clustering, and optimization. Currently, machine learning has already been widely used in the detection and analysis of FRBs (e.g. Wagstaff et al. 2016; Zhang et al. 2018; Wu et al. 2019; Yang et al. 2021; Adámek & Armour 2020; Agarwal et al. 2020; Bhatporia et al. 2023). For instance within the first CHIME/FRB catalog dataset, Chen et al. (2021) and Zhu-Ge et al. (2022) identify 188 and 117 repeater candidates from 474 non-repeating FRBs via unsupervised learning, correspondingly. Yang et al. (2023) instead discovered 145 repeater using FRB morphology as features, while Luo et al. (2022) identified dozens of repeater candidates with various supervised learning methods. Furthermore, Luo et al. (2022) found that the most prominent factors to distinguish between non-repeating and repeating FRBs are brightness temperature and rest-frame frequency bandwidth, whereas Sun et al. (2024) found spectral running may play a role instead. Furthermore, some studies have used machine learning techniques to classify thousands of bursts from highly active repeaters, such as FRB 20121102 (Raquel et al. 2023) and FRB 20201124A (Chen et al. 2023), in an effort to analyze their potential radiation mechanisms.

In addition to classifying FRBs based on their repeatability, some studies have also investigated the clustering of FRBs using characteristics beyond repeatability, as well as the empirical relationships among these features. For instance, similar to the well-known classification of GRB, where short GRBs exhibit short prompt emissions and are mostly associated with the old population, while long GRBs with long prompt emissions and are mostly associated with the young population (Zhang et al. 2007; Kumar & Zhang 2014), Guo & Wei (2022) proposed classifying FRBs based on their association with either old or young stellar populations. They discovered several tight empirical relations for non-repeaters in the first CHIME/FRB catalog, such as $\log E - \log L_\nu$, $\log E - \log DM_E$ and $\log DM_E - \log L_\nu$, where \log means the logarithm to base 10, and E , DM_E , L_ν are isotropic energy, spectral luminosity, and extragalactic DM, respectively. Similar empirical relations were found for non-repeaters associated with old populations and all non-repeaters, though with notably different slopes and intercepts, such as $\log F_\nu - \log S_\nu$, $\log DM_E - \log S_\nu$, and $\log F_\nu - \log DM_E$, where F_ν is specific fluence, S_ν is flux. Many empirical relations still hold for localized FRBs (Li et al. 2024). Based on these empirical relations, FRBs could potentially serve as standard candles, allowing cosmological models to be constrained without relying on DM measurements (Guo & Wei 2024). Li et al. (2021) classified FRBs into short ($W < 100$ ms) and long ($W > 100$ ms) bursts, where W represents the pulse width. A strong power-law correlation between fluence and peak flux density was identified for these categories. Xiao & Dai (2022) classified repeating FRBs into classical ($T_B \geq 10^{33}$ K) and atypical ($T_B < 10^{33}$ K) bursts, where T_B refers to the brightness temperature. A tight power-law correlation between pulse width and fluence was also observed for classical bursts.

CHIME has recently released a new repeater catalog (CHIME/FRB Collaboration et al. 2023), significantly increasing the data available on repeaters. This expanded dataset is expected to improve the accuracy of identifying repeater candidates through machine learning. In this paper, we will apply unsupervised learning methods to classify the FRBs from the combined data of these two catalogs into different clusters, find potential repeaters among the non-repeaters, and analyze possible empirical relations across these clusters. This paper is structured as follows. In Section 2, we present the selected CHIME data and the features used in our analysis. Section 3 introduces two types of unsupervised

machine learning methods, i.e., dimensionality reduction and clustering, as well as evaluation metrics. In Section 4, we present the results of dimensionality reduction and clustering, then we analyze the potential empirical relations. Finally, Section 5 provides our conclusions.

2. DATA SET

2.1. Sample Construction

In this paper, we use the largest available FRB data from CHIME to date, including the first CHIME/FRB Catalog (CHIME/FRB Collaboration et al. 2021, hereafter Cat1) and the CHIME/FRB Collaboration (2023) Catalog (CHIME/FRB Collaboration et al. 2023, hereafter Cat2023). The Cat1 includes 536 events (474 non-repeaters and 62 repeat bursts from 18 repeaters). There are 600 sub-bursts in total because of multiple peaks appearing in the light curve of FRB. The Cat2023 contains 127 events from 39 repeaters¹, or 151 sub-bursts for all events. Since there are 6 FRBs in Cat1 with flux and fluence values of zero, we excluded those FRBs. Additionally, 6 non-repeaters in Cat1, identified as repeaters, are duplicates in Cat2023, resulting in 739 FRB bursts used in this paper.

2.2. Feature Selection

We treat all sub-bursts as individual bursts and use their features for machine learning algorithms. To provide a more comprehensive description of an FRB event, we included a broad range of parameters based on their usage in previous research, as different studies emphasize different features and identify varying important ones (e.g. Chen et al. 2022; Luo et al. 2022; Zhu-Ge et al. 2022; Sun et al. 2024). These parameters can be divided into two categories: observational parameters (original data provided by Cat1 and Cat2023) and derived parameters, and we present the distribution of all parameters for the entire FRB dataset in Figure 1. We chose 10 observational parameters as did by Chen et al. (2022):

- Boxcar width Δt_{bc} (ms) – The boxcar width of the burst, with the label name ‘*bc_width*’ in the two catalogs.
- Width of the burst Δt_{fitb} (ms) – The width of the burst that is fitted by `fitburst`², with the label name ‘*width_fitb*’ in the two catalogs.
- Flux S_ν (Jy) – The peak flux of the band-average profile (lower limit) with the label name ‘*flux*’ in the two catalogs.
- Fluence F_ν (Jy · ms) – The flux integrated over the duration of the burst (lower limit) with the label name ‘*fluence*’ in the two catalogs.
- Scattering time Δt_{sc} (ms) – The scattering time at 600 MHz of the burst, with the label name ‘*scat_time*’ in the two catalogs.
- Spectral index γ – The spectral shape parameter of the burst. The label name in the two catalogs is ‘*sp_idx*’.
- Spectral running r – This value characterizes the frequency dependence of the spectral shape and is labeled as ‘*sp_run*’ in both catalogs.
- Highest frequency ν_{max} (MHz) – The highest frequency band of detection for the burst at full-width tenth-maximum. The label name in the two catalogs is ‘*high_freq*’.
- Lowest frequency ν_{min} (MHz) – The lowest frequency band of detection for the burst at full-width tenth-maximum. The label name in the two catalogs is ‘*low_freq*’.
- Peak frequency ν_p (MHz) – The peak frequency for the burst and is labeled as ‘*peak_freq*’ in both catalogs.

For Δt_{bc} , Δt_{fitb} , S_ν , F_ν , and Δt_{sc} , we take their logarithmic values throughout this work. Cat1 and Cat2023 only provide upper limits for the width of the burst and scattering time for some FRBs, so we opted to use these upper limits in our analysis.

For the derived parameters, we choose 6 physical properties of FRBs (see more details in Zhu-Ge et al. 2023):

¹ In fact, CHIME/FRB Collaboration et al. (2023) marked 14 FRB sources as repeater candidates due to lower significance, indicating that the burst-to-burst DM and sky position differences are larger compared to other confirmed repeaters, and their repetition rates are relatively low. In this study, we consider these 14 FRB sources as repeaters, as they warrant further follow-up observations for potential confirmation.

² <https://github.com/CHIMEFRB/fitburst>

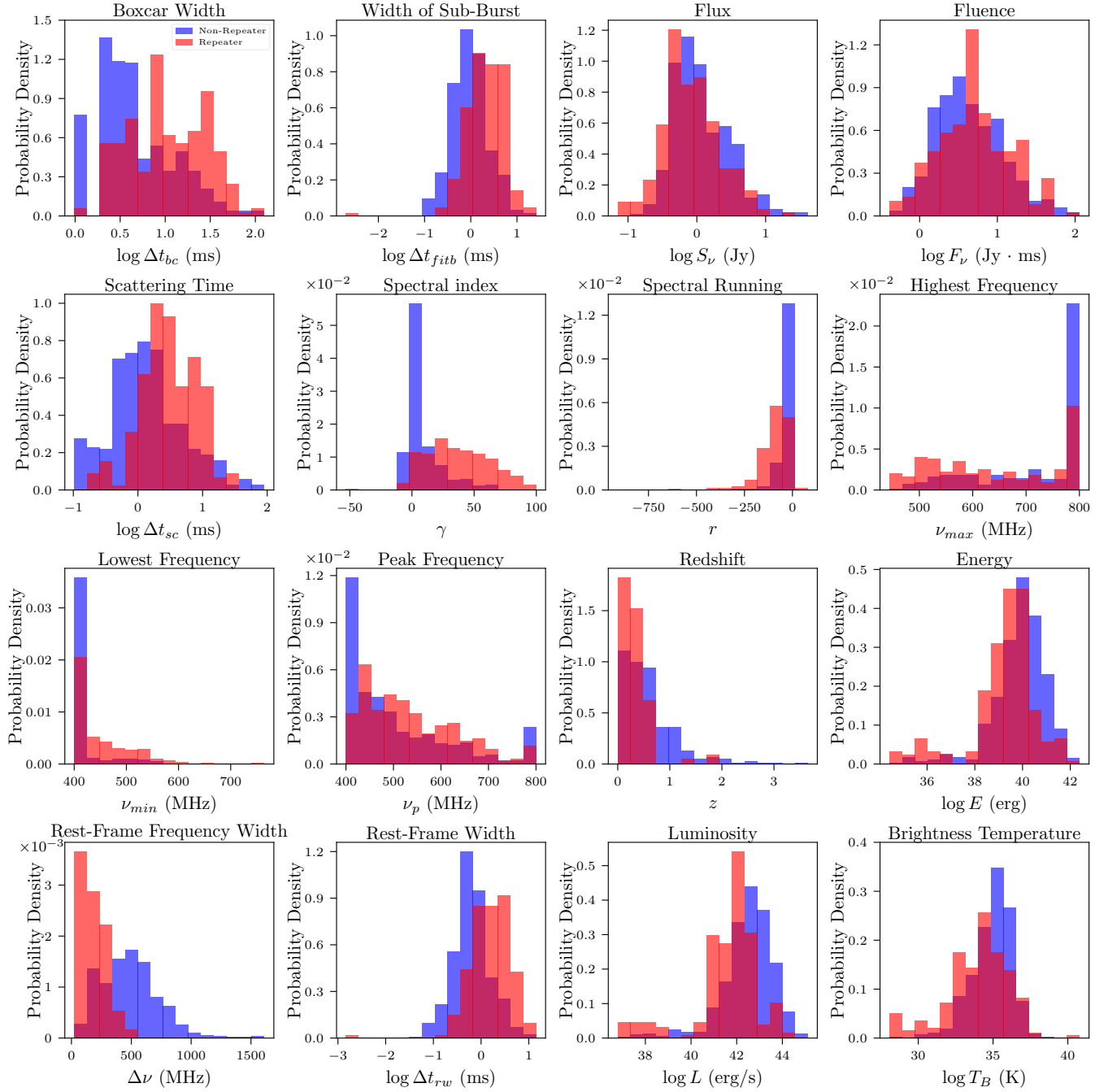


Figure 1. The distributions of observed and derived parameters for non-repeaters and repeaters are shown separately, forming the input data used for unsupervised learning. For more details, refer to Section 2.

- Redshift z – The redshift of FRBs is numerically derived from their dispersion measure (DM).

In astronomical observations, distance plays a crucial role in analyzing the origin of FRBs. The Dispersion Measure (DM), indicating the total column density of free electrons along the line of sight, serves as a key distance-related parameter. For most FRBs, DM values far exceed those predicted for the Milky Way, pointing to their extragalactic origins. The DM of FRB can be separated into different components (see e.g. Deng & Zhang 2014; Gao et al. 2014; Zhou et al. 2014; Yang et al. 2017; Yang & Zhang 2016; Li et al. 2019; Wei et al.

2019; Qiang et al. 2020; Qiang & Wei 2020, 2021; Qiang et al. 2022):

$$\text{DM}_{\text{obs}} = \text{DM}_{\text{MW}} + \text{DM}_{\text{halo}} + \text{DM}_{\text{IGM}} + \text{DM}_{\text{host}}/(1+z), \quad (1)$$

where DM_{MW} , DM_{halo} , DM_{IGM} and DM_{host} represent the contributions from the Milky Way, the Milky Way halo, the intergalactic medium (IGM), and the host galaxy (including the interstellar medium of the host galaxy and the plasma around source) of the FRB. In the literature, we usually use extragalactic DM for research

$$\text{DM}_E = \text{DM}_{\text{obs}} - \text{DM}_{\text{MW}} - \text{DM}_{\text{halo}} = \text{DM}_{\text{IGM}} + \text{DM}_{\text{host}}/(1+z). \quad (2)$$

In this paper, the values DM_{obs} are provided by both catalogs with label name ‘bonsai_dm’. We used the values of DM_{MW} as provided in Cat1 and Cat2023, which were estimated using the NE2001 model (Cordes & Lazio 2002)(the corresponding label names in Cat1 and Cat2023 are ‘dm_exc_ne2001’ and ‘dm_exc_1_ne2001’, respectively). Following the previous studies, we adopt $\text{DM}_{\text{halo}} = 30 \text{ pc cm}^{-3}$ and $\text{DM}_{\text{host}} = 70 \text{ pc cm}^{-3}$. For the DM_{IGM} , it can be written as (see e.g. Deng & Zhang 2014; Yang & Zhang 2016; Li et al. 2019; Wei et al. 2019; Qiang et al. 2020; Qiang & Wei 2020, 2021; Qiang et al. 2022)

$$\text{DM}_{\text{IGM}}(z) = \frac{3cH_0\Omega_{b,0}}{8\pi Gm_p} \int_0^z \frac{f_{\text{IGM}}(\tilde{z}) f_e(\tilde{z}) (1+\tilde{z}) d\tilde{z}}{E(\tilde{z})}, \quad (3)$$

where c is the speed of light, G is the gravitational constant, m_p is the mass of proton, $E(z)$ is the dimensionless Hubble parameter. For cosmological parameters, we adopt $H_0 = 67.4 \text{ km s}^{-1} \text{ Mpc}^{-1}$, $\Omega_m = 0.315$ and $\Omega_{b,0}h^2 = 0.0224$ from the latest Planck 18 results for the flat Λ CDM cosmology (Planck Collaboration et al. 2020). $f_e(z)$ is the ionized electron number fraction per baryon, and $f_{\text{IGM}}(z)$ is the fraction of baryon mass in IGM. In principle, these two parameters are functions of redshift z . In this work, we follow e.g. Qiang et al. (2020); Qiang & Wei (2021); Gao et al. (2014); Yang et al. (2017) and use the fiducial values $f_e = 0.875$ and $f_{\text{IGM}} = 0.83$. According to Eq.2 and Eq. 3, we can derive the redshift of all FRBs. Following Zhu-Ge et al. (2023), we also set a minimum redshift of 0.002248 corresponding to a luminosity distance of 10 Mpc to avoid zero or negative values.

- Rest-frame frequency width $\Delta\nu$ (MHz) – The frequency width corrected for the cosmological redshift effect, it can be calculated by

$$\Delta\nu = (\nu_{\text{max}} - \nu_{\text{min}})(1+z). \quad (4)$$

- Rest-frame width Δt_{rw} (ms) – The width of the burst Δt_{fitb} corrected for the cosmological redshift effect: $\Delta t_{rw} = \Delta t_{fitb}/(1+z)$. We take the logarithmic values.
- Burst energy E (erg) – The energy of a FRB can be calculated by

$$E = \frac{4\pi d_L^2}{1+z} F_\nu \nu_p, \quad (5)$$

where d_L is the luminosity distance. We take their logarithmic values.

- Luminosity L (erg/s) – The luminosity of FRBs can be derived from

$$L = 4\pi d_L^2 S_\nu \nu_p, \quad (6)$$

and we take the logarithmic values.

- Brightness temperature T_B (K) – The brightness temperature can be derived as (Luo et al. 2022)

$$T_B = \frac{S_\nu d_L^2}{2\pi\kappa_B(\nu_p \Delta t_{fitb})^2} = 1.1 \times 10^{35} \text{ K} \left(\frac{S_\nu}{\text{Jy}} \right) \left(\frac{d_L}{\text{Gpc}} \right)^2 \left(\frac{\nu_p}{\text{GHz}} \right)^{-2} \left(\frac{\Delta t_{fitb}}{\text{ms}} \right)^{-2} \frac{1}{1+z}, \quad (7)$$

where κ_B is the Boltzmann constant. We take the logarithmic values.

3. METHOD

Dimensionality reduction and clustering are two types of unsupervised machine learning methods used in this paper. First, we apply the dimensionality reduction algorithm to automatically convert high-dimensional data into low-dimensional data. Then, we use a clustering algorithm to cluster the reduced-dimensional data based on their similarities.

3.1. Machine Learning Techniques

3.1.1. Dimensionality Reduction

In this study, we use Uniform Manifold Approximation and Projection (UMAP, McInnes et al. 2018), implemented via the Python package `umap-learn`³, to perform dimensionality reduction. UMAP is a dimensionality reduction technique that can be used for both visualization and general nonlinear dimensionality reduction. This algorithm assumes that the input data is uniformly distributed on a Riemannian manifold with a locally constant (or approximately constant) Riemannian metric and that the manifold is locally connected. Based on these assumptions, the manifold can be modeled using a fuzzy topological structure.

The use of UMAP has been extensively explored in many studies (e.g. Zhu-Ge et al. 2022; Yang et al. 2023; Raquel et al. 2023; Chen et al. 2023). For FRB classification, the three parameters `n_components`, `n_neighbors`, and `min_dist` have a more significant impact on the classification results. Meanwhile, we also experimented with modifying other parameters and found that they had minimal effect on the classification outcomes. Therefore, in this study, we choose to focus on adjusting these three parameters of UMAP. `n_components` allows us to determine the dimensionality of the reduced space where the data will be embedded. In our work, we set `n_components` = 2 for all features, projecting the data onto a 2D plane for visual representation. `n_neighbors` controls how UMAP balances the local and global structure of data. UMAP achieves this by controlling the size of the local neighborhood it considers when attempting to learn the underlying structure of the data. This means that low values of `n_neighbors` will cause UMAP to focus on very local structures, potentially at the cost of missing the overall global structure. On the other hand, higher values of `n_neighbors` will push UMAP to consider larger neighborhoods around each point, capturing the broader structure of the data, but possibly losing finer details. `min_dist` decides how tightly UMAP can pack points together in low-dimensional space. Basically, it sets the minimum distance between points in the low-dimensional space. Lower values of `min_dist` will lead to more tightly packed, “clumpier” embeddings, which can be beneficial for identifying clusters or preserving finer topological details. In contrast, higher values of `min_dist` will prevent the points from being tightly packed, instead focusing on maintaining the broader topological structure. We scan `n_neighbors` from 2 to 50 and `min_dist` from 0.0 to 0.99. In this paper, we take `n_neighbors` = 21, and `min_dist` = 0.03.

3.1.2. Clustering Algorithms

In this work, we used k-means (MacQueen et al. 1967; Lloyd 1982) and Hierarchical Density-Based Spatial Clustering of Applications with Noise (HDBSCAN, Campello et al. 2013, 2015; McInnes et al. 2017) to group the reduced-dimensional data into different clusters. K-means clustering is based on the distance between each data point and its corresponding cluster center. It aims to minimize the distance between the points and their respective centers, effectively grouping similar points into clusters based on proximity in the feature space. Initially, the k-means algorithm selects k random points as the initial cluster centers, calculates the Euclidean distance of each data point from these centers, and assigns each point to the nearest center. Then, it recalculates the mean of each cluster, updating the cluster centers. This process is repeated iteratively until the cluster centers stabilize, minimizing the overall variance within the cluster (for details, see Fotopoulou 2024, and references therein). We use `sklearn.cluster.KMeans`⁴ to perform the k-means clustering algorithm. The essential hyperparameter is `n_clusters` which means how many clusters are present in the model.

HDBSCAN is a clustering algorithm developed by Campello et al. (2013, 2015). It extends Density-based Spatial Clustering of Applications with Noise (DBSCAN, Ester et al. 1996) by transforming it into a hierarchical clustering method (Han et al. 2012). The algorithm then extracts flat clusters from this hierarchy based on the stability of the clusters, which allows it to better handle varying densities and identify clusters of different shapes and sizes. HDBSCAN uses minimum spanning trees, allowing it to discover clusters with varying densities, unlike DBSCAN, which assumes a

³ <https://github.com/lmcinnes/umap>

⁴ <https://scikit-learn.org/stable/modules/generated/sklearn.cluster.KMeans.html>

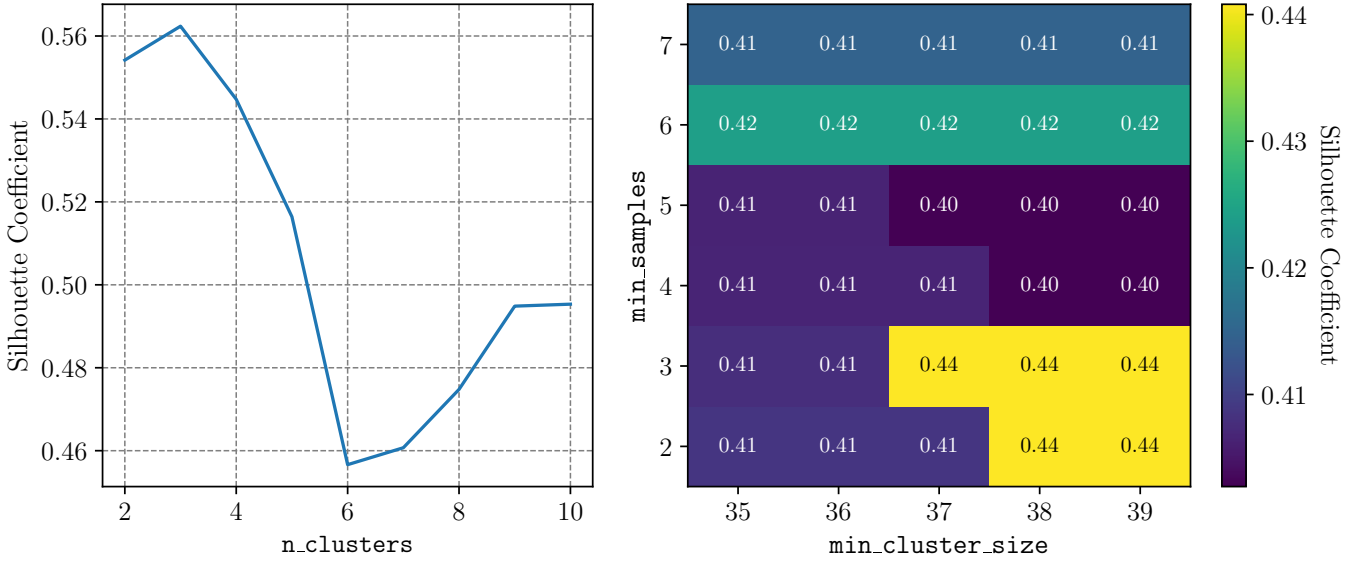


Figure 2. The mean silhouette coefficients of the k-means (left panel) and HDBSCAN (right panel) with respect to different hyperparameters.

constant density across the entire dataset. This flexibility enables HDBSCAN to identify clusters of different shapes and sizes, making it more adaptable to complex structures. We use a Python package `hdbscan`⁵ to perform this clustering algorithm. The hyperparameters of HDBSCAN adjusted in this paper are `min_cluster_size` and `min_samples`. `min_cluster_size` controls the minimum number of points required to form a cluster, while `min_samples` determines how conservative the algorithm is in classifying points as noise or part of a cluster. These parameters directly influence the number of clusters and the overall shape of the clustering.

To improve the clustering results, we optimize the hyperparameters of the clustering algorithm by maximizing the mean silhouette coefficient⁶ (Rousseeuw 1987) across all samples. The silhouette coefficient measures how well a sample fits within its assigned cluster, with values ranging from -1 to 1. Higher values indicate more tightly grouped, well-defined clusters. We show the mean silhouette coefficients changed with the hyperparameters of the clustering algorithm in Figure 2. In this work, we chose the hyperparameters with max mean silhouette coefficients, which are `n_clusters` = 3 for k-means, `min_cluster_size` = 37⁷ and `min_samples` = 3 for HDBSCAN. We also include the condensed tree of HDBSCAN in Appendix A to highlight the persistence and stability of the clustering results.

3.2. Evaluation Metrics

In this study, we experimented with various machine learning algorithms and hyperparameters, and their classification performance requires evaluation using specific metrics. The outputs of clustering can be written as the following forms:

- *TP*: The true positives, which means the number of repeaters correctly classified in the repeater cluster.
- *TN*: The true negatives, represent the number of non-repeaters correctly classified in the non-repeater cluster.
- *FP*: The false positives, represent the number of non-repeaters incorrectly classified in the repeater cluster.
- *FN*: The false negatives, indicating the number of repeaters incorrectly classified into the non-repeater cluster.

Generally, based on the four outputs mentioned above, various metrics can be calculated to evaluate the model's performance:

⁵ <https://hdbscan.readthedocs.io/en/latest/index.html>

⁶ https://scikit-learn.org/stable/modules/generated/sklearn.metrics.silhouette_score.html

⁷ In fact, when we fixed `min_samples` at 3, the mean silhouette coefficients remained constant as `min_cluster_size` varied from 37 to 60. However, the number of noise points increased during this range. Therefore, we chose `min_cluster_size` = 37 for this study.

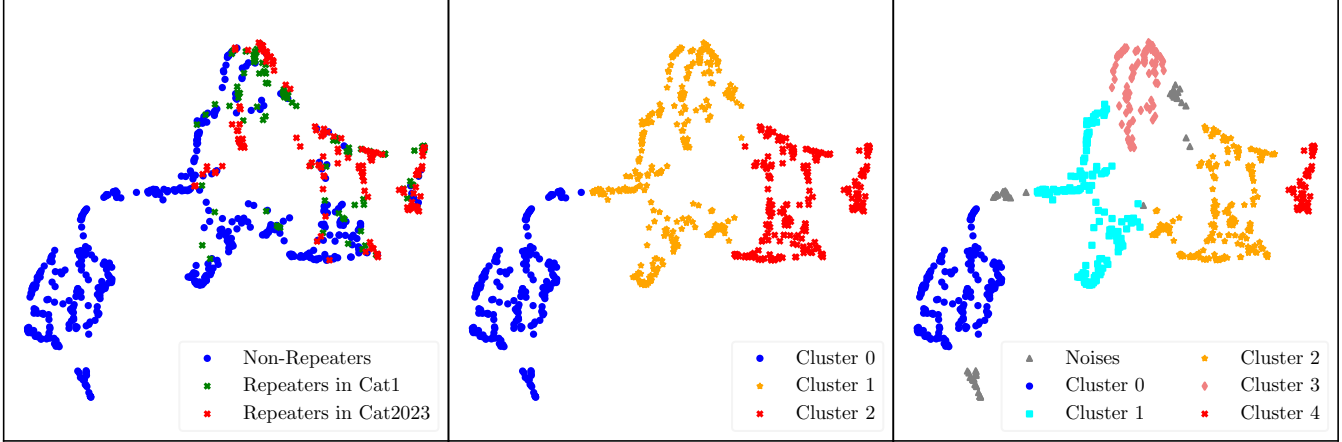


Figure 3. The results of dimensionality reduction and clustering. Left panel: The distribution of UMAP-embedded data. Blue dots represent non-repeaters, while green and red crosses indicate repeaters from Cat1 and Cat2023, respectively. Middle panel: The clustering result of UMAP-embedded data from k-means. Cluster 0, 1, and 2 are represented by blue dots, orange stars, and red crosses, respectively. Right panel: The clustering result of UMAP-embedded data from HDBSCAN. Gray triangles, blue dots, cyan squares, orange stars, light coral diamonds, and red crosses represent Noise, and Cluster 0, 1, 2, 3, and 4, respectively.

- Recall: $TP/(TP + FN)$.
- Precision: $TP/(TP + FP)$.
- Accuracy: $(TP + TN)/(TP + TN + FP + FN)$.

In this study, we use recall to evaluate the model’s performance, as observational limitations prevent the accurate determination of non-repeaters, making it impossible to reliably estimate TN and FP .

4. RESULTS AND DISCUSSION

4.1. Dimensionality reduction and clustering

Based on the methods and hyperparameters discussed in Section 3.1.1, we present the UMAP-dimensionally reduced features of 745 FRBs in the left panel of Figure 3. The blue dots represent non-repeaters, while the green and red crosses indicate repeaters from Cat1 and Cat2023, respectively. It is evident that after dimensionality reduction by UMAP, the repeaters are clustered in the upper right corner, while a distinct group of pure non-repeaters appears in the lower left corner, separated by a noticeable gap from the mixture. This indicates that the 16 parameters of FRBs used in the analysis have the ability to distinguish between non-repeaters and repeaters.

Then we used two types of clustering algorithms, k-means and HDBSCAN, to cluster the two-dimensional UMAP embedding. We present the clustering results in the middle and right panels of Figure 3, based on the hyperparameters of k-means and HDBSCAN discussed in Section 3.1.2. If the proportion of repeaters in a cluster exceeds 30%, we classify it as a “repeater cluster”, with the non-repeaters within it considered as “repeater candidates”. Conversely, if the proportion is below 30%, it is classified as an “non-repeater cluster”.

As shown in the middle panel of Figure 3, the k-means algorithm divided the UMAP-embedded data into three clusters. Cluster 0 contains 210 FRBs, all of which are non-repeaters. Cluster 2 consists of 294 FRBs, including 98 repeaters and 196 repeater candidates (the repeater burst percentage is 33.3%). Cluster 3 contains 235 FRBs, with 132 repeaters (the repeater burst percentage is 56.2%) and 103 repeater candidates. All repeaters are classified into repeater clusters, giving a recall of 100%. Out of the 509 non-repeaters, 299 repeater candidates were identified (from 269 non-repeater sources). If these repeater candidates are real, the repeater source percentage of FRBs would reach approximately 61.7%, exceeding the predicted rates from studies such as Chen et al. (2022), Zhu-Ge et al. (2022), and Yang et al. (2023).

As shown in the right panel of Figure 3, HDBSCAN divided the UMAP-embedded data into five clusters and a noise cluster. Cluster 0 contains 169 FRBs, all of which are non-repeaters. Cluster 1 includes 15 repeaters and 138

Algorithm	Clusters	Non-repeater number	Repeater number	Repeater candidate number	Total number	Repeater burst percentage	Recall	Repeater source percentage
K-means	0	210	0	0	210	0%	100%	61.7%
	1	0	98	196	294	33.3%		
	2	0	132	103	235	56.2%		
HDBSCAN	Noise	45	14	0	59	23.7%	93.5%	37.0%
	0	169	0	0	169	0%		
	1	138	15	0	153	9.8%		
	2	0	88	118	206	42.7%		
	3	0	66	28	94	70.2%		
	4	0	47	11	58	81.0%		

Table 1. The clustering results of UMAP-embedded data using k-means and HDBSCAN. For a detailed description, see Section 4.1.

non-repeaters, with repeater bursts making up only 9.8%. Clusters 2, 3, and 4 contain 206, 94, and 58 FRBs, with 88, 66, and 47 repeaters (repeater bursts percentage accounting for 42.7%, 70.2%, and 81.0%, respectively) and repeater candidates numbering 118, 28, and 11 (a total of 157 candidates, corresponding to 141 non-repeater sources). The recall for the 739 samples is 93.1%. The overall repeater source percentage is around 37.9%, slightly lower than the results of Yamasaki et al. (2023); McGregor & Lorimer (2024), but comparable to those of Chen et al. (2022), Zhu-Ge et al. (2022), and Yang et al. (2023). Detailed clustering results for both algorithms are also presented in Table 1.

We plot the feature distributions of different clusters generated by k-means and HDBSCAN in Figure 4 and Figure 5, respectively. As shown in Figure 4, the rest-frame frequency width differs the most across clusters, indicating that repeater clusters tend to have narrower frequency bandwidths. Significant differences are also observed in the distributions of the spectral index, highest frequency, redshift, energy, luminosity, and brightness temperature among the clusters. These results are consistent with the feature distribution of repeaters and non-repeaters shown in Figure 1. In Figure 5, almost all features show notable differences in their distributions among clusters, with rest-frame frequency width once again being the most distinct, similar to the results in Figure 4.

As mentioned in Section 2, there are 6 FRB sources that were previously observed as non-repeaters in Cat1 but were later identified as repeaters in Cat2023. We marked these 6 FRBs in Figure 6 with green open stars to analyze the reliability of our repeater candidate predictions. The left and right panels of Figure 6 show the repeater candidate predictions from k-means and HDBSCAN, respectively. For k-means, five out of these 6 FRB sources are located in the repeater clusters and were successfully identified as repeater candidates, while HDBSCAN predicted four of them successfully. This indicates that our method is effective in identifying potential repeaters. However, one of these 6 FRBs stands out—FRB 20180910A—which was classified into the non-repeater cluster by both clustering algorithms. After analyzing its 16 parameters, we found that its boxcar width is only 0.98 ms, and its spectral index (0.05) and spectral running (-0.53) are very similar to those of non-repeaters. Additionally, its broadband emission characteristics differ significantly from the narrow-band emission typically observed in repeaters. Currently, there is no satisfactory theoretical explanation for repeaters that exhibit characteristics so similar to non-repeaters. We also found that FRB 20180910A has so far produced three detected bursts, with intervals of 1 year and 9 months. These bursts exhibit noticeable differences in boxcar width, bandwidth, spectral index, and spectral running. It is possible that these bursts are from different non-repeaters within the same galaxy (or neighboring galaxies in the same direction). Further observations are needed to confirm this. Regarding FRB 20190226B, which was misidentified only by HDBSCAN, we analyzed its 16 parameters and found no distinct characteristics suggesting it is a non-repeating burst.

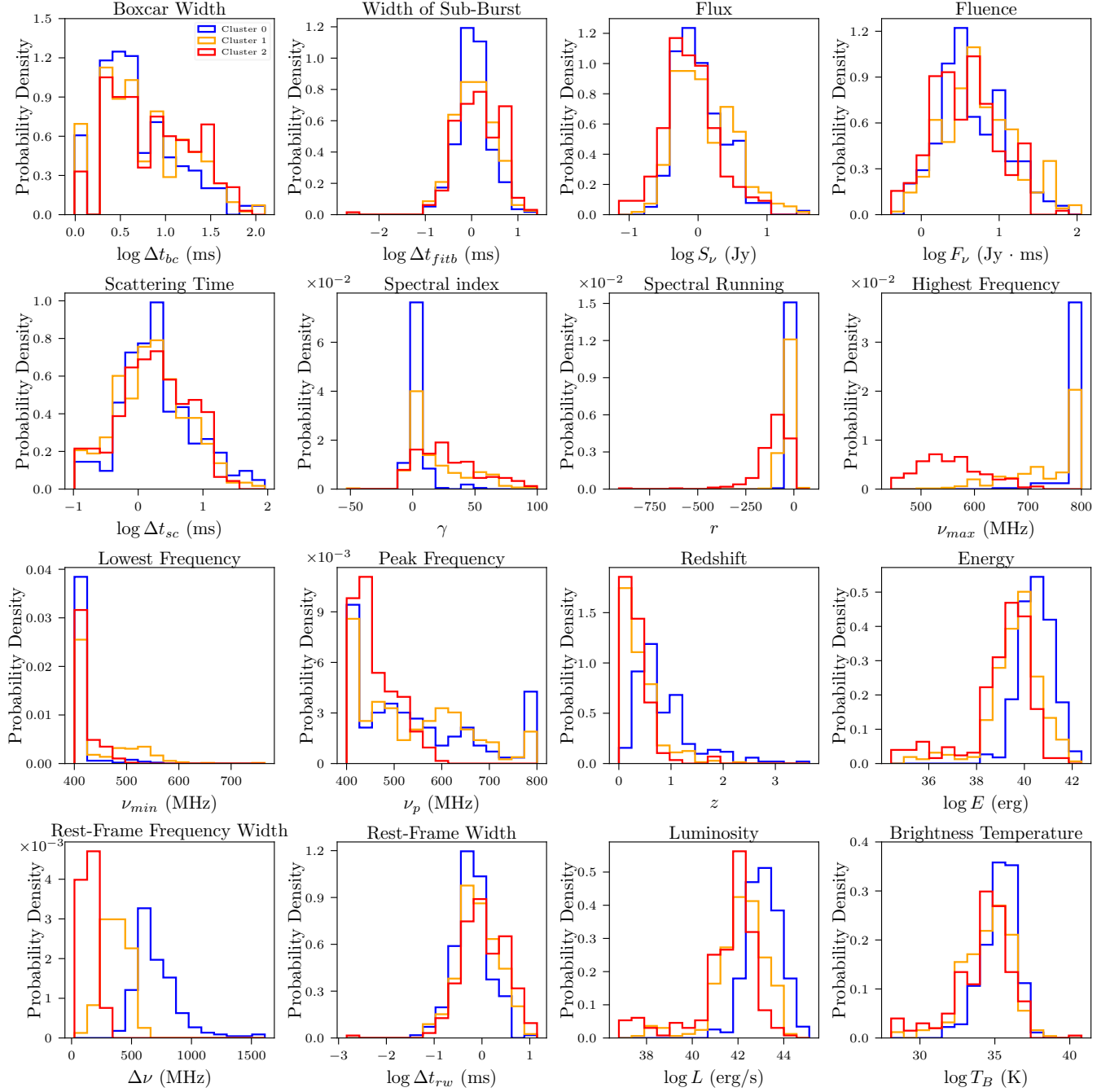


Figure 4. The distributions of 16 parameters across different clusters from k-means are illustrated, with blue, orange, and red histogram step lines representing Cluster 0, Cluster 1, and Cluster 2, respectively.

Additionally, some of the non-repeaters from Cat1 have identified host galaxies (Bhardwaj et al. 2024; Law et al. 2020). In both panels of Figure 6, we highlight two of these FRBs (FRB 20181220A and FRB 20190418A) that were identified as repeater candidates by both clustering algorithms with black circles. Continued observations of the host galaxies of these two FRBs may reveal further repeating bursts in the future.

4.2. Empirical Relationships

In this paper, we further analyze the potential two-dimensional empirical relations within different clusters identified by various clustering algorithms. We pair the 16 parameters of FRBs from different clusters and linearly fit the

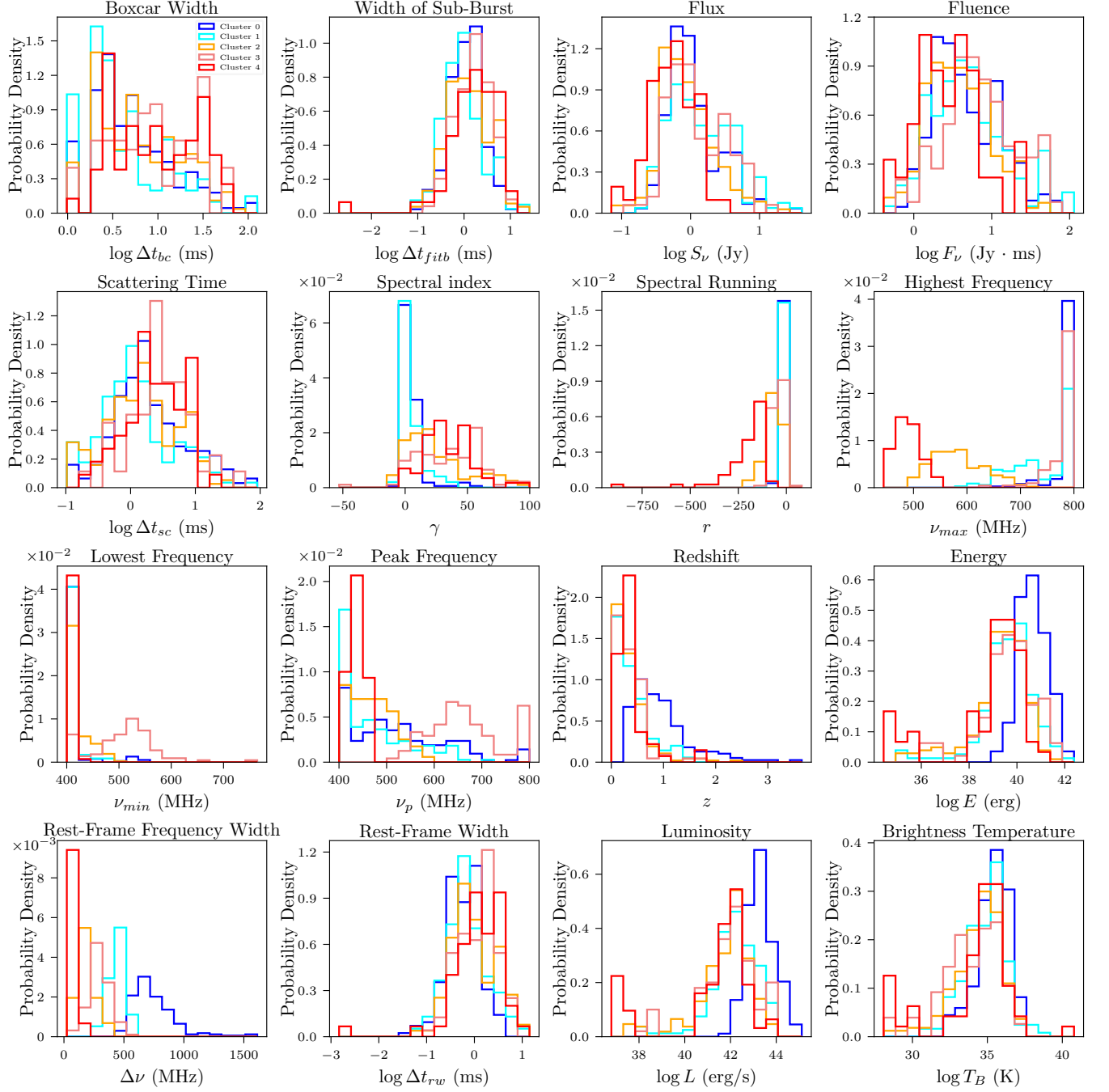


Figure 5. Same as Figure 4, but displays the results from HDBSCAN. The blue, cyan, orange, light coral, and red histogram step lines represent Cluster 0, 1, 2, 3, and 4, respectively.

data points using `scipy.stats.linregress`⁸, which performs linear least-squares regression. The form of the two-dimensional empirical relationship is given as $y = ax + b$, and the goodness of fit is evaluated using the score (coefficient of determination), defined as $R^2 = 1 - \sum_i (y_i - \hat{y}_i)^2 / \sum_i (y_i - \bar{y}_i)^2$, where y_i , \hat{y}_i , and \bar{y}_i are the observed values, the regressed values and the mean of the observed values, respectively. The closer R^2 is to 1, the better the model fits the data. To quantify the statistical differences in the slopes and intercepts of empirical relationships across different

⁸ <https://docs.scipy.org/doc/scipy/reference/generated/scipy.stats.linregress.html>

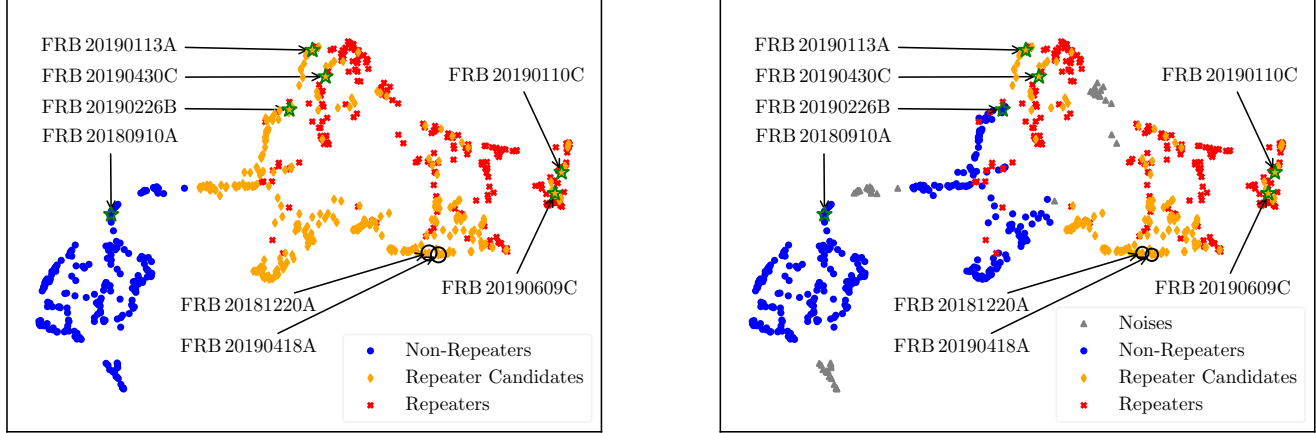


Figure 6. The distribution of non-repeaters (blue dots), repeater candidates (orange diamonds), and repeaters (red crosses) is presented in the clustered UMAP-embedded data from both k-means (left panel) and HDBSCAN (right panel). The gray triangles represent noises. The green stars mark the first bursts of six repeaters that were misidentified as non-repeaters in Cat1 but are later identified as repeaters in Cat2023. The black circles indicate the localized non-repeaters.

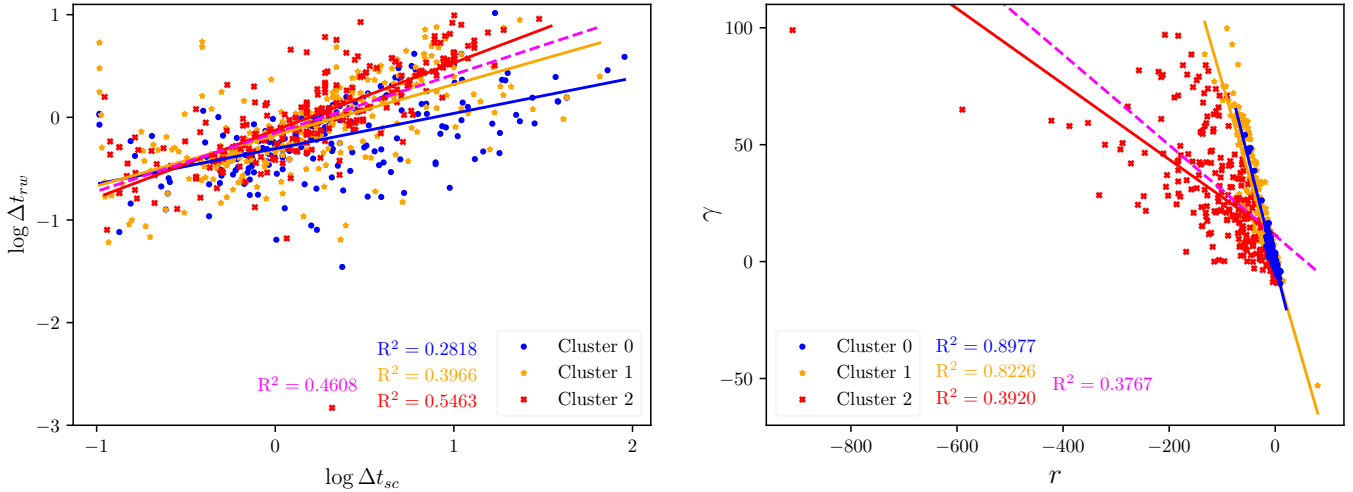


Figure 7. The empirical relationships between scattering time ($\log \Delta t_{sc}$) and rest-frame width ($\log \Delta t_{rw}$) (left panel), and between spectral acceleration (r) and spectral index (γ) (right panel) are shown for FRBs in different clusters from k-means. These relationships are represented by blue, orange, and red lines, corresponding to clusters 0, 1, and 2, respectively. The associated R^2 values are shown in the same colors. Additionally, the dashed magenta line and its corresponding R^2 represent the combined data from clusters 1 and 2. See Section 4.2 for details.

clusters, we implemented the Chow test for evaluation (Chow 1960). The null hypothesis of the Chow test is that the two samples come from the same regression model. If the p -value is less than 0.05, the null hypothesis is rejected, indicating that the two samples come from different regression models.

We set a high score threshold of $R^2 > 0.5$ to filter out well-fitted empirical relations and excluded parameter combinations that inherently have a linear relationship (e.g., luminosity and flux). For the clusters from k-means, the selected empirical relations are shown in Figure 7. The slope, intercept, and score of the empirical relations are listed in Table 2. The p -values of the Chow test between different clusters are listed in Table 3. The left panel of Figure 7 shows the empirical relation between two independent parameters: scattering time ($\log \Delta t_{sc}$) and rest-frame width ($\log \Delta t_{rw}$). We observe that $R^2 > 0.5$ only in cluster 2, corresponding to a repeater cluster, whereas the $\log \Delta t_{sc} - \log \Delta t_{rw}$ relation appears less significant in the other two clusters. However, the slope and intercept of the relation $\log \Delta t_{sc} - \log \Delta t_{rw}$ are similar in clusters 1 and 2. Similarly, the p -value of the Chow test between clusters 1 and 2 is greater than 0.05, indicating that they likely come from the same regression model. This may be

x	y	Clusters	a	b	R^2
$\log \Delta t_{sc}$	$\log \Delta t_{rw}$	0	0.3440	-0.3055	0.2818
		1	0.4954	-0.1744	0.3966
		2	0.6572	-0.1256	0.5463
		[1, 2]	0.5691	-0.1519	0.4608
r	γ	0	-0.9000	-1.6846	0.8977
		1	-0.7853	-1.9914	0.8226
		2	-0.1613	11.4422	0.3920
		[1, 2]	-0.1936	11.1439	0.3767

Table 2. The slope (a), intercept (b), and R^2 values of the empirical relations for different clusters from k-means.

Clusters	p-value	Relation	
		$\log \Delta t_{sc} - \log \Delta t_{rw}$	$r - \gamma$
0 & 1	0.0016	0.5177	
0 & 2	1.75e-06	6.28e-05	
1 & 2	0.1975	1.11e-16	
0 & [1, 2]	2.49e-06	0.0190	

Table 3. The p -values of Chow tests for k-means clusters.

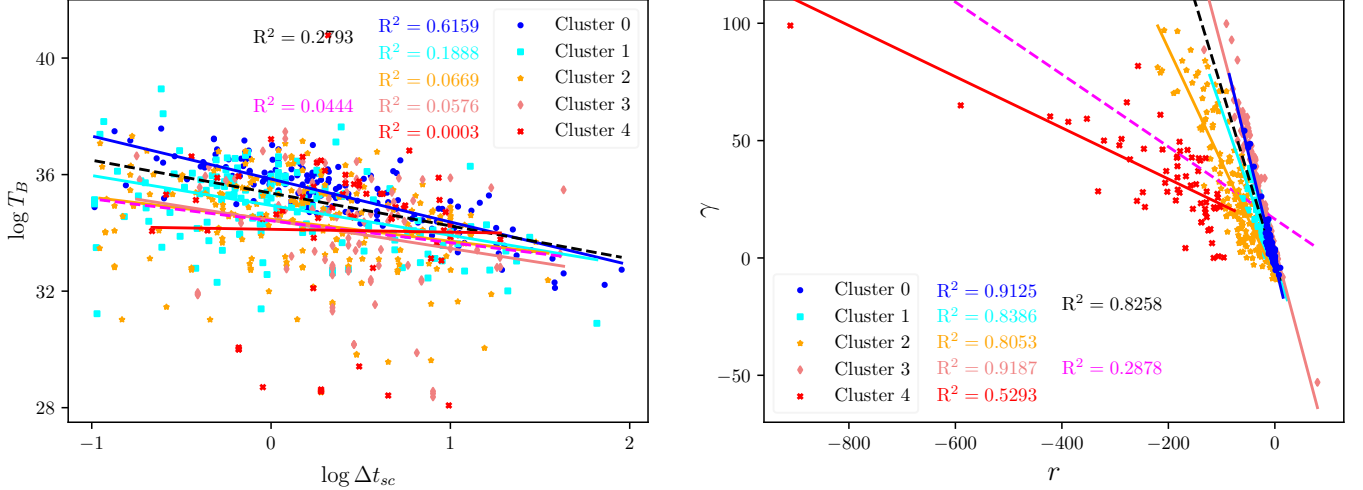


Figure 8. The empirical relationships between scattering time ($\log \Delta t_{sc}$) and brightness temperature ($\log T_B$) (left panel), and between spectral acceleration (r) and spectral index (γ) (right panel) are shown for FRBs in different clusters from HDBSCAN. These relationships are represented by blue, cyan, orange, light coral, and red lines, corresponding to clusters 0, 1, 2, 3, and 4, respectively. The associated R^2 values are shown in the same colors. Additionally, the dashed black (magenta) line and its corresponding R^2 represent the combined data from clusters 0 and 1 (2, 3, and 4). See Section 4.2 for details.

because both clusters are repeater clusters. The right panel of Figure 7 displays the empirical relation between two other independent parameters: spectral acceleration (r) and spectral index (γ). In contrast to the $\log \Delta t_{rw} - \log \Delta t_{sc}$ relation, the $r - \gamma$ relation is less evident in cluster 2, but is very pronounced in clusters 0 and 1 ($R^2 > 0.8$), with similar slopes and intercepts. Moreover, the p -value of the Chow test between these two clusters even reaches around 0.5, indicating that some repeaters may share spectral properties with non-repeaters. Combining the two repeater clusters, cluster 1 and cluster 2, the relation $\log \Delta t_{sc} - \log \Delta t_{rw}$ yields an R^2 value of 0.4608. Although this is less

x	y	Clusters	a	b	R^2
$\log \Delta t_{sc}$	$\log T_B$	0	-1.4741	35.8475	0.6159
		1	-1.0264	34.9418	0.1888
		2	-0.7559	34.4684	0.0669
		3	-0.9667	34.4318	0.0576
		4	-0.098	34.1223	0.0003
		[0, 1]	-1.1274	35.3659	0.2793
		[2, 3, 4]	-0.7510	34.4152	0.0444
r	γ	0	-0.9394	-2.2495	0.9125
		1	-0.6574	-2.6236	0.8386
		2	-0.4835	-7.4780	0.8053
		3	-0.8527	4.4482	0.9187
		4	-0.1090	11.8615	0.5293
		[0, 1]	-0.7424	-2.1286	0.8258
		[2, 3, 4]	-0.1542	16.5526	0.2878

Table 4. The slope (a), intercept (b), and R^2 values of the empirical relations for different clusters from HDBSCAN.

p -value \ Relation	$\log \Delta t_{sc} - \log T_B$	$r - \gamma$
Clusters		
0 & 1	0.0041	1.13e-10
0 & 2	0.1701	1.75e-09
0 & 3	0.0483	0.4561
0 & 4	0.5232	1.11e-16
1 & 2	0.2403	0.0019
1 & 3	8.12e-07	6.34e-12
1 & 4	0.0014	1.11e-16
2 & 3	0.0002	1.11e-16
2 & 4	0.0379	1.11e-16
3 & 4	0.6024	1.11e-16
[0, 1] & [2, 3, 4]	2.43e-11	1.97e-08

Table 5. The p -values of Chow tests for HDBSCAN clusters.

than 0.5, it still exhibits a distinct empirical correlation compared to non-repeating bursts. The $r - \gamma$ relation for the combined clusters has an R^2 value of 0.3767, which is even lower than that of cluster 2. This may result from the substantial disparity between the $r - \gamma$ relations of cluster 1 and cluster 2, as well as the relatively weak correlation observed in cluster 2. The p -values of the Chow test between the non-repeater cluster (Cluster 0) and the repeater clusters (Clusters 1 and 2) are all below 0.05 for both empirical relations. This result strengthens the idea that FRBs can be classified into repeaters and non-repeaters.

Figure 8 shows the empirical relations for different clusters from HDBSCAN, and Table 4 lists the slope, intercept, and score of these empirical relations. The left panel displays the relation between rest-frame width ($\log \Delta t_{sc}$) and the brightness temperature ($\log T_B$), which are also two independent parameters. We can see that only cluster 0 (a non-repeater cluster) has a significant $\log \Delta t_{sc} - \log T_B$ relation with $R^2 > 0.6$, while the other clusters show no strong $\log \Delta t_{sc} - \log T_B$ relation. Even if the p -values of the Chow test between some clusters are greater than 0.05, it does not necessarily indicate that they originate from the same regression model. The right panel shows the empirical relation between spectral acceleration (r) and spectral index (γ). All clusters exhibit a significant $r - \gamma$ relation,

especially clusters 0-3, where $R^2 > 0.8$. Notably, clusters 0 and 3 (a repeater cluster) have very similar slopes and intercepts for the $r - \gamma$ relation (the p -value of the Chow test is 0.45), suggesting that certain repeaters might have spectral properties similar to those of non-repeaters, a trend also observed in the k-means results. We also analyzed the relations using the combined data from clusters 0 and 1 (non-repeater clusters), as well as from clusters 2, 3, and 4 (repeater clusters). For the $\log \Delta t_{sc} - \log T_B$ relation, the R^2 value for the non-repeater clusters is less than 0.5, likely due to the scattered data in cluster 1. However, it still performs better than the repeater cluster, which has an R^2 value of 0.0444, indicating that the $\log \Delta t_{sc} - \log T_B$ relation is virtually non-existent for the repeater cluster. The $r - \gamma$ relation is still apparent in the non-repeater clusters, but the R^2 value is less than 0.5 in the repeater clusters. This may be due to the significant differences in slope and intercept of the $r - \gamma$ relation across clusters 2, 3, and 4. The p -values of the Chow test between non-repeater clusters and repeater clusters are all significantly below 0.05 for both empirical relations, aligning with the results from k-means clustering.

5. CONCLUSION AND FUTURE PROSPECT

Machine learning is a powerful tool to classify FRBs. In this paper, we applied unsupervised learning methods, including dimensionality reduction and clustering algorithms, to differentiate between repeaters and non-repeaters in the first CHIME/FRB catalog (CHIME/FRB Collaboration et al. 2021) and the CHIME/FRB Collaboration (2023) catalog (CHIME/FRB Collaboration et al. 2023). We extracted 16 parameters from the FRBs to serve as input features for unsupervised learning, ensuring that the information from the FRBs was sufficiently comprehensive. Ultimately, we successfully identified several candidate repeaters among the non-repeaters. Using the UMAP+k-means method, we identified 269 non-repeaters as repeater candidates, with an estimated repeater source percentage of 61.7%. With the UMAP+HDBSCAN method, 141 non-repeaters were identified as repeater candidates, yielding a repeater source percentage of 37.9%. All repeater candidates are summarized in Appendix B. Additionally, we found that FRBs in repeater clusters and non-repeater clusters exhibit different distributions across several features, suggesting that repeaters and non-repeaters may belong to distinct categories.

We used six FRB sources previously classified as non-repeaters but actually confirmed as repeaters to evaluate the predictive capability of our model. The UMAP + k-means method successfully predicted five of these sources, while the UMAP + HDBSCAN method successfully predicted four. The only exception was FRB 20180910A, which could not be predicted. The reason for this is that many of its characteristics, such as frequency bandwidth, spectral index, and spectral running, closely resemble those of non-repeaters, making it distinctly different from typical repeaters. Additionally, the intervals between the three outbursts of this repeater are quite long, and the features of each burst show significant variation. This may indicate that the FRB sources are unrelated and originate from different galaxies within the same direction or from different sources in the same galaxy. Furthermore, within Cat1, there are some localized non-repeaters, and we identified two of them as repeater candidates using both clustering algorithms. Continued observations of the host galaxies of these two FRBs may reveal additional repeating bursts in the future.

We further analyzed the empirical relations that may exist within different clusters. For the clusters derived from k-means, we identified a significant (with $R^2 > 0.5$) $\log \Delta t_{sc} - \log \Delta t_{rw}$ relation exclusive to cluster 2, as well as a $r - \gamma$ relation present only in clusters 0 and 1. For the clusters obtained through HDBSCAN, we found a notable $\log \Delta t_{sc} - \log T_B$ relation that exists solely in cluster 0, along with the $r - \gamma$ relation observed across all clusters. The spectral index γ and the spectral running r are the shape parameters of the FRB spectrum, described by a continuous power-law function (Pleunis et al. 2021; Planck Collaboration et al. 2020):

$$I(\nu) = A(\nu/\nu_0)^{\gamma+r \ln(\nu/\nu_0)}, \quad (8)$$

where $I(\nu)$ is the intensity at spectral frequency ν , A is the amplitude, and ν_0 is the pivotal frequency, set at 400.1953125 MHz, the lower limit of the CHIME band. The strict $r - \gamma$ relation means that only one parameter can determine the morphology of FRB. Some clusters from k-means exhibit relatively weak but still noteworthy empirical relations, such as the $\log \Delta t_{sc} - \log \Delta t_{rw}$ relation in clusters 0 and 1 and the $r - \gamma$ relation in cluster 2. Similarly, for HDBSCAN, the $\log \Delta t_{sc} - \log T_B$ relation is present but weak in cluster 1, while it is extremely weak in clusters 2, 3, and 4, suggesting that it is effectively nonexistent in the latter. These results suggest that the $\log \Delta t_{sc} - \log \Delta t_{rw}$ relation is more pronounced in repeater clusters, whereas the $\log \Delta t_{sc} - \log T_B$ relation is more evident in non-repeater clusters. While the $r - \gamma$ relation is significant in both repeaters and non-repeaters, the noticeable differences in slopes and intercepts across different repeater clusters indicate that repeaters do not form a homogeneous group, and their properties may vary significantly.

We also applied the Chow test to assess statistical differences in the slopes and intercepts of empirical relationships across different clusters. For certain prominent empirical relationships, the Chow test p -values indicate that some repeater and non-repeater clusters share a common regression model, such as the $r - \gamma$ relation in clusters 0 and 1 from k-means and clusters 0 and 3 from HDBSCAN. This suggests that some repeaters and non-repeaters exhibit comparable spectral characteristics, a finding consistent with observational evidence—particularly in the case of FRB 20180910A, if it is indeed a genuine repeater. However, this also implies that if some repeaters behave similarly to non-repeaters in key spectral relationships, some FRBs currently classified as non-repeaters might actually be repeaters with undetected bursts due to observational limitations. Subsequently, when all repeater and non-repeater clusters are merged separately, the Chow test p -values reveal significantly distinct empirical relationships between the two groups, reinforcing the notion that FRBs can indeed be categorized into repeaters and non-repeaters.

In the future, improvements in observational data and machine learning techniques will refine FRB classification, reduce misclassifications, and uncover more repeaters. The use of advanced clustering algorithms and multi-wavelength observations will enhance the accuracy of models, while deep learning approaches may reveal new patterns. These advancements will contribute to a better understanding of the origins and physical mechanisms of FRBs, with potential implications for cosmology.

20 We are grateful to Hao Wei, Jing-Yi Jia, Lin-Yu Li, Jia-Lei Niu, and Yu-Xuan Li for their kind assistance and valuable
 21 discussions. D.-C.Q. is supported by the Startup Research Fund of Henan Academy of Sciences No.241841222. S.Y.
 22 acknowledges the funding from the National Natural Science Foundation of China under grant No. 12303046, and
 23 the Startup Research Fund of Henan Academy of Sciences No.241841217. J.Z. is supported by the funding from the
 24 National Natural Science Foundation of China under grant No.12403002, and the Startup Research Fund of Henan
 25 Academy of Sciences No.241841221. Z.-Q.Y. is supported by the National Natural Science Foundation of China under
 26 grant No. 12305059, the Joint Fund of Henan Province Science and Technology R&D Program No.235200810111, and
 27 the Startup Research Fund of Henan Academy of Sciences No.241841224.

REFERENCES

- Adámek, K., & Armour, W. 2020, ApJS, 247, 56,
 doi: [10.3847/1538-4365/ab7994](https://doi.org/10.3847/1538-4365/ab7994)
- Agarwal, D., Aggarwal, K., Burke-Spoliar, S., Lorimer, D. R., & Garver-Daniels, N. 2020, MNRAS, 497, 1661,
 doi: [10.1093/mnras/staa1856](https://doi.org/10.1093/mnras/staa1856)
- Bhardwaj, M., Michilli, D., Kirichenko, A. Y., et al. 2024,
 ApJL, 971, L51, doi: [10.3847/2041-8213/ad64d1](https://doi.org/10.3847/2041-8213/ad64d1)
- Bhatporia, S., Walters, A., Murugan, J., & Weltman, A. 2023, arXiv e-prints, arXiv:2311.03456,
 doi: [10.48550/arXiv.2311.03456](https://doi.org/10.48550/arXiv.2311.03456)
- Breiman, L. 2001, Machine Learning, 45, 5,
 doi: [10.1023/A:1010933404324](https://doi.org/10.1023/A:1010933404324)
- Burke-Spoliar, S., & Bannister, K. W. 2014, Astrophys. J., 792, 19, doi: [10.1088/0004-637X/792/1/19](https://doi.org/10.1088/0004-637X/792/1/19)
- Campello, R. J. G. B., Moulavi, D., & Sander, J. 2013, in Advances in Knowledge Discovery and Data Mining, ed. J. Pei, V. S. Tseng, L. Cao, H. Motoda, & G. Xu (Berlin, Heidelberg: Springer Berlin Heidelberg), 160–172
- Campello, R. J. G. B., Moulavi, D., Zimek, A., & Sander, J. 2015, ACM Trans. Knowl. Discov. Data, 10,
 doi: [10.1145/2733381](https://doi.org/10.1145/2733381)
- Chang, C.-C., & Lin, C.-J. 2011, ACM Trans. Intell. Syst. Technol., 2, doi: [10.1145/1961189.1961199](https://doi.org/10.1145/1961189.1961199)
- Chen, B. H., Hashimoto, T., Goto, T., et al. 2021, Mon. Not. Roy. Astron. Soc., 509, 1227,
 doi: [10.1093/mnras/stab2994](https://doi.org/10.1093/mnras/stab2994)
- Chen, B. H., Hashimoto, T., Goto, T., et al. 2022, MNRAS, 509, 1227, doi: [10.1093/mnras/stab2994](https://doi.org/10.1093/mnras/stab2994)
- Chen, B. H., Hashimoto, T., Goto, T., et al. 2023, Mon. Not. Roy. Astron. Soc., 521, 5738,
 doi: [10.1093/mnras/stad930](https://doi.org/10.1093/mnras/stad930)
- CHIME/FRB Collaboration, Amiri, M., Bandura, K., et al. 2018, ApJ, 863, 48, doi: [10.3847/1538-4357/aad188](https://doi.org/10.3847/1538-4357/aad188)
- CHIME/FRB Collaboration, Amiri, M., Andersen, B. C., et al. 2021, ApJS, 257, 59,
 doi: [10.3847/1538-4365/ac33ab](https://doi.org/10.3847/1538-4365/ac33ab)
- CHIME/FRB Collaboration, Andersen, B. C., Bandura, K., et al. 2023, ApJ, 947, 83, doi: [10.3847/1538-4357/acc6c1](https://doi.org/10.3847/1538-4357/acc6c1)
- Chow, G. C. 1960, Econometrica, 28, 591.
<http://www.jstor.org/stable/1910133>
- Cordes, J. M., & Lazio, T. J. W. 2002, arXiv e-prints,
 astro, doi: [10.48550/arXiv.astro-ph/0207156](https://doi.org/10.48550/arXiv.astro-ph/0207156)
- Cover, T., & Hart, P. 1967, IEEE Trans. Inf. Theor., 13, 21–27, doi: [10.1109/TIT.1967.1053964](https://doi.org/10.1109/TIT.1967.1053964)

- Dempster, A. P., Laird, N. M., & Rubin, D. B. 2018, Journal of the Royal Statistical Society: Series B (Methodological), 39, 1, doi: [10.1111/j.2517-6161.1977.tb01600.x](https://doi.org/10.1111/j.2517-6161.1977.tb01600.x)
- Deng, W., & Zhang, B. 2014, *Astrophys. J. Lett.*, 783, L35, doi: [10.1088/2041-8205/783/2/L35](https://doi.org/10.1088/2041-8205/783/2/L35)
- Ester, M., Kriegel, H.-P., Sander, J., Xu, X., et al. 1996in , 226–231
- Fonseca, E., Andersen, B. C., Bhardwaj, M., et al. 2020, *ApJL*, 891, L6, doi: [10.3847/2041-8213/ab7208](https://doi.org/10.3847/2041-8213/ab7208)
- Fotopoulou, S. 2024, *Astronomy and Computing*, 48, 100851, doi: [10.1016/j.ascom.2024.100851](https://doi.org/10.1016/j.ascom.2024.100851)
- Gao, H., Li, Z., & Zhang, B. 2014, *Astrophys. J.*, 788, 189, doi: [10.1088/0004-637X/788/2/189](https://doi.org/10.1088/0004-637X/788/2/189)
- Gordon, A. C., Fong, W.-f., Kilpatrick, C. D., et al. 2023, *ApJ*, 954, 80, doi: [10.3847/1538-4357/ace5aa](https://doi.org/10.3847/1538-4357/ace5aa)
- Guo, H.-Y., & Wei, H. 2022, *JCAP*, 07, 010, doi: [10.1088/1475-7516/2022/07/010](https://doi.org/10.1088/1475-7516/2022/07/010)
- . 2024, *Phys. Lett. B*, 859, 139120, doi: [10.1016/j.physletb.2024.139120](https://doi.org/10.1016/j.physletb.2024.139120)
- Hallinan, G., Ravi, V., Weinreb, S., et al. 2019, in *Bulletin of the American Astronomical Society*, Vol. 51, 255, doi: [10.48550/arXiv.1907.07648](https://doi.org/10.48550/arXiv.1907.07648)
- Han, J., Kamber, M., & Pei, J. 2012, in *Data Mining* (Third Edition), third edition edn., ed. J. Han, M. Kamber, & J. Pei, The Morgan Kaufmann Series in Data Management Systems (Boston: Morgan Kaufmann), 443–495, doi: <https://doi.org/10.1016/B978-0-12-381479-1.00010-1>
- Jankowski, F., Bezuidenhout, M. C., Caleb, M., et al. 2023, *MNRAS*, 524, 4275, doi: [10.1093/mnras/stad2041](https://doi.org/10.1093/mnras/stad2041)
- Keane, E. F. 2018, *Nature Astron.*, 2, 865, doi: [10.1038/s41550-018-0603-0](https://doi.org/10.1038/s41550-018-0603-0)
- Kirsten, F., Marcote, B., Nimmo, K., et al. 2022, *Nature*, 602, 585, doi: [10.1038/s41586-021-04354-w](https://doi.org/10.1038/s41586-021-04354-w)
- Kocz, J., Ravi, V., Catha, M., et al. 2019, *MNRAS*, 489, 919, doi: [10.1093/mnras/stz2219](https://doi.org/10.1093/mnras/stz2219)
- Kumar, P., & Zhang, B. 2014, *Phys. Rept.*, 561, 1, doi: [10.1016/j.physrep.2014.09.008](https://doi.org/10.1016/j.physrep.2014.09.008)
- Kumar, P., Shannon, R. M., Osłowski, S., et al. 2019, *ApJL*, 887, L30, doi: [10.3847/2041-8213/ab5b08](https://doi.org/10.3847/2041-8213/ab5b08)
- Law, C. J., Butler, B. J., Prochaska, J. X., et al. 2020, *ApJ*, 899, 161, doi: [10.3847/1538-4357/aba4ac](https://doi.org/10.3847/1538-4357/aba4ac)
- Law, C. J., Sharma, K., Ravi, V., et al. 2024, *ApJ*, 967, 29, doi: [10.3847/1538-4357/ad3736](https://doi.org/10.3847/1538-4357/ad3736)
- Li, D., & Pan, Z. 2016, *Radio Science*, 51, 1060, doi: [10.1002/2015RS005877](https://doi.org/10.1002/2015RS005877)
- Li, L.-Y., Jia, J.-Y., Qiang, D.-C., & Wei, H. 2024, arXiv e-prints, arXiv:2408.12983, doi: [10.48550/arXiv.2408.12983](https://doi.org/10.48550/arXiv.2408.12983)
- Li, X. J., Dong, X. F., Zhang, Z. B., & Li, D. 2021, *Astrophys. J.*, 923, 230, doi: [10.3847/1538-4357/ac3085](https://doi.org/10.3847/1538-4357/ac3085)
- Li, Z., Gao, H., Wei, J.-J., et al. 2019, *Astrophys. J.*, 876, 146, doi: [10.3847/1538-4357/ab18fe](https://doi.org/10.3847/1538-4357/ab18fe)
- Lloyd, S. 1982, *IEEE transactions on information theory*, 28, 129
- Lorimer, D. R. 2018, *Nature Astron.*, 2, 860, doi: [10.1038/s41550-018-0607-9](https://doi.org/10.1038/s41550-018-0607-9)
- Lorimer, D. R., Bailes, M., McLaughlin, M. A., Narkevic, D. J., & Crawford, F. 2007, *Science*, 318, 777, doi: [10.1126/science.1147532](https://doi.org/10.1126/science.1147532)
- Luo, J.-W., Zhu-Ge, J.-M., & Zhang, B. 2022, *Mon. Not. Roy. Astron. Soc.*, 518, 1629, doi: [10.1093/mnras/stac3206](https://doi.org/10.1093/mnras/stac3206)
- MacQueen, J., et al. 1967in , Oakland, CA, USA, 281–297
- McGregor, K., & Lorimer, D. R. 2024, *Astrophys. J.*, 961, 10, doi: [10.3847/1538-4357/ad1184](https://doi.org/10.3847/1538-4357/ad1184)
- McInnes, L., Healy, J., & Astels, S. 2017, *Journal of Open Source Software*, 2, 205, doi: [10.21105/joss.00205](https://doi.org/10.21105/joss.00205)
- McInnes, L., Healy, J., & Melville, J. 2018, <https://arxiv.org/abs/1802.03426>
- Niu, C. H., Aggarwal, K., Li, D., et al. 2022, *Nature*, 606, 873, doi: [10.1038/s41586-022-04755-5](https://doi.org/10.1038/s41586-022-04755-5)
- Petroff, E., Hessels, J. W. T., & Lorimer, D. R. 2022, *Astron. Astrophys. Rev.*, 30, 2, doi: [10.1007/s00159-022-00139-w](https://doi.org/10.1007/s00159-022-00139-w)
- Petroff, E., Keane, E. F., Barr, E. D., et al. 2015, *MNRAS*, 451, 3933, doi: [10.1093/mnras/stv1242](https://doi.org/10.1093/mnras/stv1242)
- Petroff, E., Barr, E. D., Jameson, A., et al. 2016, *Publ. Astron. Soc. Austral.*, 33, e045, doi: [10.1017/pasa.2016.35](https://doi.org/10.1017/pasa.2016.35)
- Planck Collaboration, Aghanim, N., Akrami, Y., et al. 2020, *A&A*, 641, A6, doi: [10.1051/0004-6361/201833910](https://doi.org/10.1051/0004-6361/201833910)
- Pleunis, Z., Good, D. C., Kaspi, V. M., et al. 2021, *ApJ*, 923, 1, doi: [10.3847/1538-4357/ac33ac](https://doi.org/10.3847/1538-4357/ac33ac)
- Qiang, D.-C., Deng, H.-K., & Wei, H. 2020, *Class. Quant. Grav.*, 37, 185022, doi: [10.1088/1361-6382/ab7f8e](https://doi.org/10.1088/1361-6382/ab7f8e)
- Qiang, D.-C., Li, S.-L., & Wei, H. 2022, *JCAP*, 01, 040, doi: [10.1088/1475-7516/2022/01/040](https://doi.org/10.1088/1475-7516/2022/01/040)
- Qiang, D.-C., & Wei, H. 2020, *JCAP*, 04, 023, doi: [10.1088/1475-7516/2020/04/023](https://doi.org/10.1088/1475-7516/2020/04/023)
- . 2021, *Phys. Rev. D*, 103, 083536, doi: [10.1103/PhysRevD.103.083536](https://doi.org/10.1103/PhysRevD.103.083536)
- Raquel, B. J. R., Hashimoto, T., Goto, T., et al. 2023, *Mon. Not. Roy. Astron. Soc.*, 524, 1668, doi: [10.1093/mnras/stad1942](https://doi.org/10.1093/mnras/stad1942)
- Ravi, V. 2019, *Nature Astron.*, 3, 928, doi: [10.1038/s41550-019-0831-y](https://doi.org/10.1038/s41550-019-0831-y)
- Ravi, V., & Lasky, P. D. 2014, *Mon. Not. Roy. Astron. Soc.*, 441, 2433, doi: [10.1093/mnras/stu720](https://doi.org/10.1093/mnras/stu720)

- Rousseeuw, P. J. 1987, Journal of Computational and Applied Mathematics, 20, 53,
doi: [https://doi.org/10.1016/0377-0427\(87\)90125-7](https://doi.org/10.1016/0377-0427(87)90125-7)
- Rumelhart, D. E., Hinton, G. E., & Williams, R. J. 1986, Nature, 323, 533, doi: [10.1038/323533a0](https://doi.org/10.1038/323533a0)
- Shannon, R. M., Bannister, K. W., Bera, A., et al. 2024, arXiv e-prints, arXiv:2408.02083,
doi: [10.48550/arXiv.2408.02083](https://doi.org/10.48550/arXiv.2408.02083)
- Sharma, K., Ravi, V., Connor, L., et al. 2024, Nature, 635, 61, doi: [10.1038/s41586-024-08074-9](https://doi.org/10.1038/s41586-024-08074-9)
- Spitler, L. G., Cordes, J. M., Hessels, J. W. T., et al. 2014, ApJ, 790, 101, doi: [10.1088/0004-637X/790/2/101](https://doi.org/10.1088/0004-637X/790/2/101)
- Spitler, L. G., Scholz, P., Hessels, J. W. T., et al. 2016, Nature, 531, 202, doi: [10.1038/nature17168](https://doi.org/10.1038/nature17168)
- Sun, W.-P., Zhang, J.-G., Li, Y., et al. 2024.
<https://arxiv.org/abs/2409.11173>
- Thornton, D., Stappers, B., Bailes, M., et al. 2013, Science, 341, 53, doi: [10.1126/science.1236789](https://doi.org/10.1126/science.1236789)
- Vapnik, V. 1999, IEEE Transactions on Neural Networks, 10, 988, doi: [10.1109/72.788640](https://doi.org/10.1109/72.788640)
- Wagstaff, K. L., Tang, B., Thompson, D. R., et al. 2016, PASP, 128, 084503,
doi: [10.1088/1538-3873/128/966/084503](https://doi.org/10.1088/1538-3873/128/966/084503)
- Wang, B., & Wei, J.-J. 2023, Astrophys. J., 944, 50,
doi: [10.3847/1538-4357/acb2c8](https://doi.org/10.3847/1538-4357/acb2c8)
- Wang, F. Y., Wang, Y. Y., Yang, Y.-P., et al. 2020a,
Astrophys. J., 891, 72, doi: [10.3847/1538-4357/ab74d0](https://doi.org/10.3847/1538-4357/ab74d0)
- Wang, F. Y., & Zhang, G. Q. 2019, Astrophys. J., 882, 108,
doi: [10.3847/1538-4357/ab35dc](https://doi.org/10.3847/1538-4357/ab35dc)
- Wang, W.-Y., Xu, R., & Chen, X. 2020b, Astrophys. J., 899, 109, doi: [10.3847/1538-4357/aba268](https://doi.org/10.3847/1538-4357/aba268)
- Wei, J.-J., Li, Z., Gao, H., & Wu, X.-F. 2019, JCAP, 09, 039, doi: [10.1088/1475-7516/2019/09/039](https://doi.org/10.1088/1475-7516/2019/09/039)
- Wu, D., Cao, H., Lv, N., et al. 2019, ApJL, 887, L10,
doi: [10.3847/2041-8213/ab595e](https://doi.org/10.3847/2041-8213/ab595e)
- Xiao, D., & Dai, Z.-G. 2022, Astron. Astrophys., 657, L7,
doi: [10.1051/0004-6361/202142268](https://doi.org/10.1051/0004-6361/202142268)
- Xiao, D., Wang, F., & Dai, Z. 2021, Sci. China Phys. Mech. Astron., 64, 249501, doi: [10.1007/s11433-020-1661-7](https://doi.org/10.1007/s11433-020-1661-7)
- . 2022, Fast Radio Bursts, ed. C. Bambi & A. Santangelo (Singapore: Springer Nature Singapore), 1–38,
doi: [10.1007/978-981-16-4544-0_128-1](https://doi.org/10.1007/978-981-16-4544-0_128-1)
- Xu, H., Niu, J. R., Chen, P., et al. 2022, Nature, 609, 685,
doi: [10.1038/s41586-022-05071-8](https://doi.org/10.1038/s41586-022-05071-8)
- Xu, J., Feng, Y., Li, D., et al. 2023, Universe, 9, 330,
doi: [10.3390/universe9070330](https://doi.org/10.3390/universe9070330)
- Yamasaki, S., Goto, T., Ling, C.-T., & Hashimoto, T. 2023,
Mon. Not. Roy. Astron. Soc., 527, 11158,
doi: [10.1093/mnras/stad3844](https://doi.org/10.1093/mnras/stad3844)
- Yang, X., Zhang, S. B., Wang, J. S., & Wu, X. F. 2023,
Mon. Not. Roy. Astron. Soc., 522, 4342,
doi: [10.1093/mnras/stad1304](https://doi.org/10.1093/mnras/stad1304)
- Yang, X., Zhang, S. B., Wang, J. S., et al. 2021, MNRAS,
507, 3238, doi: [10.1093/mnras/stab2275](https://doi.org/10.1093/mnras/stab2275)
- Yang, Y.-P., Luo, R., Li, Z., & Zhang, B. 2017, Astrophys. J. Lett., 839, L25, doi: [10.3847/2041-8213/aa6c2e](https://doi.org/10.3847/2041-8213/aa6c2e)
- Yang, Y.-P., & Zhang, B. 2016, Astrophys. J. Lett., 830, L31, doi: [10.3847/2041-8205/830/2/L31](https://doi.org/10.3847/2041-8205/830/2/L31)
- Zhang, B. 2014, Astrophys. J. Lett., 780, L21,
doi: [10.1088/2041-8205/780/2/L21](https://doi.org/10.1088/2041-8205/780/2/L21)
- Zhang, B., Zhang, B.-B., Liang, E.-W., et al. 2007,
Astrophys. J. Lett., 655, L25, doi: [10.1086/511781](https://doi.org/10.1086/511781)
- Zhang, M.-J., & Li, H. 2018, Eur. Phys. J. C, 78, 460,
doi: [10.1140/epjc/s10052-018-5953-3](https://doi.org/10.1140/epjc/s10052-018-5953-3)
- Zhang, R. C., & Zhang, B. 2022, Astrophys. J. Lett., 924, L14, doi: [10.3847/2041-8213/ac46ad](https://doi.org/10.3847/2041-8213/ac46ad)
- Zhang, R. C., Zhang, B., Li, Y., & Lorimer, D. R. 2021,
Mon. Not. Roy. Astron. Soc., 501, 157,
doi: [10.1093/mnras/staa3537](https://doi.org/10.1093/mnras/staa3537)
- Zhang, Y. G., Gajjar, V., Foster, G., et al. 2018, ApJ, 866, 149, doi: [10.3847/1538-4357/aadf31](https://doi.org/10.3847/1538-4357/aadf31)
- Zhou, B., Li, X., Wang, T., Fan, Y.-Z., & Wei, D.-M. 2014,
Phys. Rev. D, 89, 107303,
doi: [10.1103/PhysRevD.89.107303](https://doi.org/10.1103/PhysRevD.89.107303)
- Zhu-Ge, J.-M., Luo, J.-W., & Zhang, B. 2022, Mon. Not. Roy. Astron. Soc., 519, 1823,
doi: [10.1093/mnras/stac3599](https://doi.org/10.1093/mnras/stac3599)
- Zhu-Ge, J.-M., Luo, J.-W., & Zhang, B. 2023, MNRAS,
519, 1823, doi: [10.1093/mnras/stac3599](https://doi.org/10.1093/mnras/stac3599)

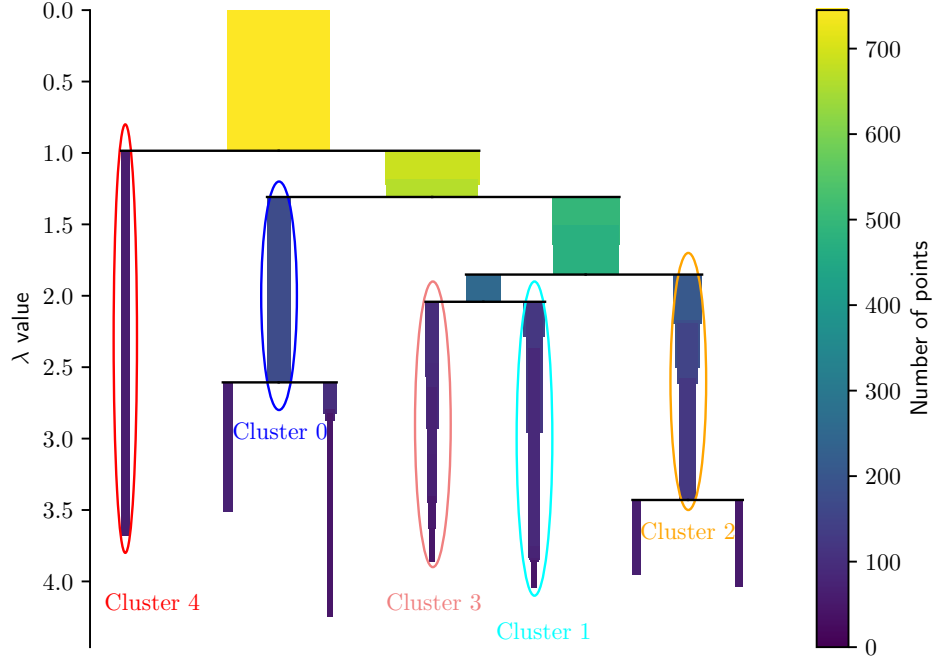


Figure 9. The condensed tree of HDBSCAN. The leaf nodes within ellipses of different colors represent the final clusters obtained by HDBSCAN, other leaf nodes are noise.

APPENDIX

A. CONDENSED TREE OF HDBSCAN

We show the condensed tree of HDBSCAN in Figure 9 to highlight the persistence and stability of the clustering results. λ is used to consider the persistence of clusters, which can be calculated by $\lambda = 1/d$, where d is the distance between a point and cluster core. For a given cluster, λ_{birth} marks when the cluster first formed, and λ_{death} (if applicable) marks when it split into smaller clusters. For each point p in the cluster, λ_p represents the value at which the point left the cluster, occurring between λ_{birth} and λ_{death} , either during the cluster's lifetime or at the split. Then we can compute the stability for each cluster as $S = \sum_{p \in \text{cluster}} (\lambda_p - \lambda_{\text{birth}})$. Start by declaring all leaf nodes as selected clusters. Move up the tree: if the sum of child cluster stabilities exceeds the parent cluster's stability, update the parent's stability to this sum. Otherwise, select the parent cluster and deselect its descendants. At the root node, the selected clusters form the flat clustering, which is then returned. Ultimately, we selected the five clusters enclosed within the ellipses in the Figure 9. See https://hdbscan.readthedocs.io/en/latest/how_hdbscan_works.html for more details.

B. REPEATER CANDIDATES

Here, we present the repeater candidates identified using unsupervised machine learning methods. The ‘Sub num’ column lists the sub-burst numbers of FRBs from the Cat1 and Cat2023. The ‘Note’ column specifies whether each candidate was identified exclusively by k-means ('k') or by both k-means and HDBSCAN ('both').

Table 6. The list of repeater candidates

FRB name	Sub num	RA(J2000) ($^{\circ}$)	DEC(J2000) ($^{\circ}$)	Δt_{bc} (ms)	Δt_{fitb} (ms)	S_{ν} (Jy)	F_{ν} (Jy · ms)	Δt_{sc} (ms)	γ	r	ν_{max} (MHz)	ν_{min} (MHz)	ν_{peak} (MHz)	z	$\log E$ (erg)	$\Delta \nu$ (MHz)	Δtrw (ms)	$\log L$ (erg/s)	$\log T_B$ (K)	Note
FRB20180725A	0	93.4	67.1	2.95	0.30	1.70	4.10	1.10	38.20	-45.80	760.1	485.3	607.4	0.641	40.45	450.9	0.18	43.28	35.74	k
FRB20180729A	0	199.4	55.6	0.98	0.10	11.70	17.00	0.16	16.46	-30.21	692.7	400.2	525.6	0.002	36.03	293.2	0.10	38.87	32.69	k
FRB20180729B	0	89.9	56.5	1.97	0.31	0.92	1.20	0.66	14.50	-14.60	800.2	441.8	657.5	0.158	38.70	414.9	0.27	41.64	34.50	k
FRB20180801A	0	322.5	72.7	9.83	0.58	1.11	7.90	5.54	60.00	-75.50	709.3	500.2	595.6	0.553	40.60	324.8	0.37	42.94	34.40	both
FRB20180810B	0	180.4	83.1	0.98	0.31	5.20	7.90	0.20	-0.76	-4.06	778.6	400.2	400.2	0.031	37.86	390.1	0.30	40.70	34.86	k
FRB20180812A	0	19.3	80.8	7.86	1.30	0.93	5.40	2.81	-2.90	-8.30	586.4	400.2	400.2	0.727	40.50	321.6	0.75	42.97	35.10	both
FRB20180904A	0	286.6	81.2	1.97	0.53	3.80	6.00	0.55	12.12	-23.18	712.3	400.2	519.7	0.257	39.73	392.2	0.42	42.63	35.76	k
FRB20180907A	0	320.9	29.5	5.90	0.87	0.87	2.80	0.26	-2.30	-5.10	648.6	400.2	400.2	0.797	40.30	446.5	0.48	43.04	35.40	k
FRB20180907E	0	167.9	47.1	11.80	4.15	0.73	6.90	3.38	-7.10	-2.70	536.3	400.2	400.2	0.312	39.85	178.5	3.16	41.99	33.89	both
FRB20180909A	0	123.6	56.8	19.66	6.31	0.33	1.02	8.20	-0.30	-1.30	800.2	400.2	400.2	0.319	39.04	527.5	4.79	41.67	33.12	k
FRB20180911A	0	99.5	84.6	1.97	0.83	1.60	2.60	0.94	-5.78	0.20	599.9	400.2	400.2	0.085	38.26	216.6	0.77	41.09	34.62	both
FRB20180915A	0	280.6	17.9	4.92	0.80	2.30	6.20	0.88	6.50	-9.10	800.2	400.2	571.9	0.128	39.16	451.1	0.71	41.78	34.04	k
FRB20180915B	0	225.2	25.0	4.92	1.69	0.99	3.80	0.11	-9.20	3.00	527.4	400.2	400.2	0.072	38.28	136.3	1.58	40.73	33.47	both
FRB20180916A	0	349.0	80.3	0.98	0.10	2.40	4.50	0.19	2.41	-8.10	793.2	400.2	464.7	0.151	39.08	452.2	0.09	41.87	35.79	k
FRB20180920A	0	78.9	28.3	14.75	2.22	0.86	8.50	9.10	20.10	-26.30	787.4	435.9	585.9	0.360	40.24	478.2	1.63	42.38	33.57	k
FRB20180920B	0	191.1	63.5	10.81	2.33	0.35	1.70	1.73	12.30	-121.00	483.4	400.2	421.1	0.401	39.49	116.5	1.66	41.95	33.83	both
FRB20180921A	0	28.9	5.0	3.93	1.14	0.92	2.30	1.50	1.00	-10.40	672.2	400.2	419.9	0.319	39.42	358.8	0.86	42.14	34.92	k
FRB20180922A	0	342.3	69.7	2.95	0.81	2.60	7.70	0.31	-4.00	-9.20	555.9	400.2	400.2	0.383	40.08	215.3	0.58	42.75	35.83	both
FRB20180923A	0	327.6	71.9	1.97	0.15	0.76	1.20	0.21	18.20	-57.40	572.9	400.2	468.9	0.026	36.96	177.2	0.15	39.77	33.12	both
FRB20180923D	0	169.1	48.8	0.98	0.10	2.40	2.20	0.11	20.90	-92.70	524.4	400.2	448.0	0.248	39.20	155.0	0.08	42.33	36.27	both
FRB20180923C	0	239.1	22.9	1.97	0.32	0.89	1.37	0.50	1.00	-10.20	675.6	400.2	420.5	0.059	37.69	291.7	0.30	40.53	34.01	both
FRB20180925B	0	145.4	21.0	5.90	1.15	0.76	2.70	1.40	15.00	-41.50	606.9	400.2	479.6	0.623	40.14	335.5	0.71	42.80	34.97	both
FRB20180928A	0	312.9	30.9	2.95	0.27	1.34	2.50	0.15	-2.93	-39.70	492.1	400.2	400.2	0.002	35.08	92.1	0.27	37.81	31.02	both
FRB20181012B	0	206.3	64.2	3.93	0.56	0.49	1.44	0.26	20.90	-154.00	483.9	400.2	428.3	0.682	39.90	140.8	0.33	42.66	35.31	both
FRB20181013A	0	262.8	38.4	0.98	0.51	2.81	3.50	0.56	1.08	-5.20	800.2	400.2	443.7	0.204	39.22	481.5	0.43	42.20	36.16	k
FRB20181013E	0	307.3	69.0	2.95	0.86	0.62	2.03	1.10	-5.60	0.90	623.0	400.2	400.2	0.208	38.96	269.1	0.71	41.52	34.66	both
FRB20181013B	0	97.2	52.0	119.93	2.80	0.56	21.00	65.60	-0.50	-4.20	790.4	400.2	400.2	0.119	39.47	436.5	2.50	40.95	30.90	k
FRB20181013C	0	146.1	34.1	4.92	0.76	0.44	1.64	0.43	-3.70	-0.80	698.0	400.2	400.2	0.001	40.26	595.8	0.38	42.99	35.46	k
FRB20181014C	0	117.9	41.6	3.93	0.79	0.57	1.48	1.00	18.00	-30.50	707.7	408.6	537.7	0.694	40.03	506.7	0.47	42.84	35.20	k
FRB20181017B	0	237.8	78.5	12.78	2.31	1.06	6.50	4.30	61.00	-77.00	704.8	499.3	593.2	0.207	39.63	248.0	1.91	41.92	33.27	k
FRB20181018B	0	336.8	71.9	0.98	0.48	5.10	7.90	0.50	7.30	-10.45	800.2	400.2	567.4	0.105	39.09	441.9	0.43	41.94	35.62	k
FRB20181018C	0	67.2	37.6	0.98	0.48	2.40	3.30	0.51	-0.61	-7.60	668.2	400.2	400.2	0.208	39.17	323.8	0.39	42.11	36.21	both
FRB20181022C	0	141.6	83.8	3.93	0.80	0.91	3.20	0.68	2.90	-14.20	664.2	400.2	443.9	0.456	39.30	384.3	0.55	42.52	35.19	k
FRB20181022D	0	179.2	36.5	1.97	0.59	2.90	6.20	0.63	18.20	-14.40	800.2	505.7	754.7	0.473	40.46	433.8	0.40	43.29	35.87	both
FRB20181022E	0	221.2	27.1	2.95	0.40	0.69	2.08	0.63	8.70	-42.30	560.3	400.2	443.7	0.207	39.01	193.3	0.33	41.61	34.61	both
FRB20181027A	0	131.9	-4.2	5.90	0.72	4.90	22.00	4.72	-0.40	6.10	800.2	530.0	800.2	0.662	41.33	449.2	0.43	43.90	35.39	both
FRB20181030C	0	309.8	4.0	0.98	0.61	1.60	5.50	0.74	10.00	-22.20	691.2	400.2	500.9	0.587	40.42	461.7	0.38	43.08	36.76	k
FRB20181030D	0	81.8	16.1	2.95	0.36	2.74	5.90	0.87	1.51	-3.00	800.2	400.2	514.8	0.086	38.74	434.4	0.33	41.45	34.30	k
FRB20181030E	0	135.7	8.9	5.90	0.40	2.00	6.30	0.97	22.30	-69.00	564.8	400.2	470.5	0.013	37.09	166.8	0.39	39.59	31.99	both
FRB20181101A	0	21.3	53.9	30.47	6.03	0.50	10.70	10.00	16.40	-37.70	636.8	400.2	497.4	0.413	41.46	571.0	2.50	43.51	34.03	k
FRB20181115A	0	143.0	56.4	4.92	1.83	0.44	1.92	2.10	19.60	-62.00	568.4	400.2	468.8	0.972	40.37	331.7	0.93	43.03	35.30	both
FRB20181116A	0	36.0	4.5	1.97	0.44	4.00	5.23	0.47	2.37	-11.00	704.7	400.2	445.8	0.271	39.65	387.2	0.35	42.64	35.96	k
FRB20181116B	0	232.7	64.9	3.93	0.64	0.74	1.92	0.17	-8.80	-4.70	505.5	400.2	400.2	0.336	39.36	140.6	0.48	42.07	34.92	both
FRB20181117B	1	81.1	80.0	7.86	1.28	3.60	11.00	1.30	11.40	-31.20	630.4	400.2	480.4	0.449	40.46	333.7	0.88	43.14	35.10	both
FRB20181119B	0	299.4	31.1	22.61	3.33	4.50	94.00	16.59	2.72	-4.65	800.2	400.2	536.4	0.087	39.98	434.9	3.06	41.69	32.72	k
FRB20181119C	0	190.1	82.2	0.98	0.45	2.80	3.50	0.48	-1.81	-5.70	657.7	400.2	400.2	0.178	39.06	303.4	0.38	42.03	36.13	both
FRB20181122A	0	60.0	55.5	2.95	0.68	0.53	1.42	0.18	-4.90	0.60	661.4	400.2	400.2	0.442	39.48	376.7	0.47	42.21	35.27	k
FRB20181122B	0	281.1	85.0	0.98	0.25	14.70	22.00	0.14	4.86	-13.27	729.1	400.2	480.7	0.093	39.36	359.5	0.23	42.22	36.12	k
FRB20181123A	0	300.8	55.9	1.97	0.58	0.99	2.50	1.92	25.60	-64.30	590.2	404.2	488.5	0.697	40.22	315.7	0.34	43.04	36.12	both
FRB20181125A	0	147.9	33.9	14.75	1.28	0.39	3.20	1.50	9.00	-54.00	533.7	400.2	434.5	0.171	39.02	156.3	1.09	41.17	32.81	both
FRB20181125A	1	147.9	33.9	14.75	1.44	0.39	3.20	1.50	7.30	-41.80	552.0	400.2	436.6	0.171	39.02	177.8	1.23	41.17	32.81	both
FRB20181126A	0	262.1	81.2	1.97</																

Table 6 (*continued*)

FRB name	Sub num	RA(J2000) ($^{\circ}$)	DEC(J2000) ($^{\circ}$)	Δt_{bc} (ms)	Δt_{fitb} (ms)	S_{ν} (Jy)	F_{ν} (Jy · ms)	Δt_{sc} (ms)	γ	r	ν_{max} (MHz)	ν_{min} (MHz)	ν_{peak} (MHz)	z	$\log E$ (erg)	$\Delta\nu$ (MHz)	Δtrw (ms)	$\log L$ (erg/s)	$\log T_B$ (K)	Note
FRB20181215A	0	93.4	39.3	4.92	1.34	0.34	0.72	1.70	-2.40	-1.10	800.2	400.2	400.2	0.231	38.60	492.4	1.09	41.37	34.05	k
FRB20181216A	0	306.3	53.5	1.97	0.22	0.94	1.70	0.89	14.80	-16.10	800.2	434.2	634.0	0.362	39.58	498.3	0.16	42.45	35.29	k
FRB20181218A	0	5.1	71.3	5.90	1.39	0.83	1.59	0.22	19.00	-83.60	529.3	400.2	448.4	1.894	40.82	373.6	0.48	44.00	36.00	both
FRB20181218B	0	18.0	69.4	2.95	1.69	0.56	1.80	2.00	-2.70	-2.30	708.8	400.2	400.2	0.573	39.81	485.6	1.07	42.50	35.52	k
FRB20181218C	0	286.0	58.2	4.92	5.20	0.25	1.73	6.80	4.40	-13.10	718.5	400.2	472.7	0.273	39.20	405.3	4.08	41.47	33.92	k
FRB20181219C	0	17.8	14.1	2.95	1.26	0.21	0.57	0.53	-1.00	-4.60	735.5	400.2	400.2	0.605	39.36	538.0	0.79	42.13	35.14	k
FRB20181220A	0	346.1	48.4	2.95	0.43	1.33	3.00	0.46	-5.26	-1.30	596.4	400.2	400.2	0.002	35.16	196.6	0.43	37.81	31.02	both
FRB20181220B	0	277.4	84.9	1.97	0.56	2.90	3.80	0.62	0.45	-4.80	800.2	400.2	419.5	0.134	38.86	453.7	0.49	41.80	35.25	k
FRB20181221A	0	230.6	25.9	4.92	0.75	1.25	5.80	1.32	62.10	-128.00	583.3	446.1	510.1	0.240	39.65	170.2	0.61	42.07	34.44	both
FRB20181221B	0	306.3	81.0	2.95	1.04	0.97	3.30	1.10	25.30	-61.20	597.6	405.4	492.2	1.419	40.94	465.0	0.43	43.80	36.36	k
FRB20181222D	0	188.2	56.2	22.61	3.75	0.22	1.23	1.95	8.40	-41.10	561.3	400.2	443.0	1.481	40.51	399.8	1.51	43.15	34.07	both
FRB20181222E	0	50.6	87.0	3.93	0.25	1.12	5.50	0.79	5.13	-19.90	639.5	400.2	455.2	0.212	39.46	290.0	0.21	41.86	34.57	both
FRB20181222E	1	50.6	87.0	3.93	0.91	1.12	5.50	0.79	9.90	-23.80	672.3	400.2	492.8	0.212	39.50	329.8	0.75	41.89	34.50	k
FRB20181223B	0	174.9	21.6	8.85	1.57	0.68	4.10	3.50	33.30	-41.00	761.2	473.8	606.0	0.525	40.27	438.2	1.03	42.67	34.22	k
FRB20181223C	0	181.1	27.6	1.97	0.51	1.36	2.84	0.11	2.68	-7.40	800.2	400.2	479.2	0.002	35.21	400.9	0.51	37.89	31.23	k
FRB20181224A	0	355.1	44.6	1.97	0.39	4.30	3.30	0.40	3.85	-6.08	800.2	400.2	549.5	0.160	39.07	464.0	0.33	42.25	35.34	k
FRB20181224E	0	239.3	7.3	1.97	1.06	3.60	10.30	1.10	-1.18	-4.40	729.5	400.2	400.2	0.530	40.50	504.0	0.69	43.23	36.61	k
FRB20181225B	0	36.8	88.2	2.95	1.30	1.90	7.50	1.40	6.80	-10.10	800.2	400.2	560.7	0.179	39.54	471.7	1.10	42.01	34.72	k
FRB20181226C	0	349.1	44.9	3.93	0.63	0.88	2.70	1.98	-1.09	-1.90	800.2	400.2	400.2	0.268	39.31	507.0	0.50	41.92	34.79	k
FRB20181226D	0	120.2	22.2	1.97	0.57	1.89	3.00	0.62	0.44	-5.20	800.2	400.2	417.2	0.274	39.39	509.6	0.45	42.30	35.70	k
FRB20181226B	0	182.7	12.4	1.97	0.59	8.90	52.00	1.10	4.10	-14.40	687.5	400.2	461.1	0.201	40.40	345.2	0.49	42.71	36.01	k
FRB20181226B	1	182.7	12.4	1.97	0.87	8.90	52.00	1.10	1.03	-7.00	764.2	400.2	430.7	0.201	40.37	437.3	0.72	42.68	36.07	k
FRB20181226B	2	182.7	12.4	1.97	1.00	8.90	52.00	1.10	11.50	-18.10	784.9	400.2	549.7	0.201	40.47	462.2	0.84	42.79	35.86	k
FRB20181226E	0	303.6	73.6	2.95	1.17	0.48	1.35	1.30	-5.80	-3.40	558.3	400.2	400.2	0.178	38.64	186.2	0.99	41.26	34.41	both
FRB20181228B	0	250.4	63.9	4.92	0.10	0.40	1.67	1.16	59.30	-353.00	471.8	401.5	435.2	0.512	39.72	106.3	0.07	42.28	34.76	both
FRB20181229B	0	238.4	19.8	20.64	3.36	0.42	4.90	5.10	22.00	-10.30	517.5	400.2	445.5	0.320	39.77	154.8	2.55	41.83	33.09	both
FRB20181230A	0	346.7	83.4	34.41	1.64	0.94	18.00	41.00	33.00	-27.80	800.2	543.5	724.8	0.704	41.25	437.4	0.96	43.20	33.28	both
FRB20181231B	0	128.8	56.0	2.95	0.34	0.89	2.34	1.75	59.60	-60.00	800.0	540.6	657.7	0.066	38.22	276.6	0.32	40.82	33.37	both
FRB20181231C	0	197.1	69.2	1.97	0.39	0.68	1.20	0.41	0.41	-9.60	667.0	400.2	408.8	0.503	39.53	400.9	0.26	42.46	35.82	k
FRB20190101B	0	307.8	29.9	2.95	0.32	1.02	4.40	5.16	41.70	-36.10	800.2	554.3	713.6	1.139	41.05	526.0	0.15	43.74	35.88	both
FRB20190102A	0	9.3	26.7	3.93	0.82	1.12	4.20	0.99	28.90	-67.80	595.5	411.9	495.2	0.653	40.39	303.6	0.50	43.03	35.51	both
FRB20190102B	0	21.7	21.4	2.95	0.85	1.71	3.90	0.93	0.60	-4.40	800.2	400.2	428.8	0.281	39.54	512.2	0.66	42.29	35.31	k
FRB20190103B	0	93.6	19.7	31.46	5.83	0.68	12.90	5.40	7.70	-16.30	738.4	400.2	507.0	0.313	40.23	444.1	4.44	42.07	32.81	k
FRB20190106A	0	22.2	46.1	6.88	0.94	0.27	0.81	5.80	9.00	-5.00	800.2	493.5	800.2	0.192	38.79	365.5	0.79	41.38	32.89	both
FRB20190106B	0	335.6	46.1	1.97	0.58	1.70	3.80	0.60	16.58	-68.00	543.5	400.2	452.1	0.098	38.61	157.3	0.53	41.30	34.67	both
FRB20190107A	0	0.9	21.8	47.19	25.90	0.49	6.30	20.40	-4.30	-0.40	666.9	400.2	400.2	0.824	40.68	486.5	14.20	42.83	33.38	k
FRB20190107B	0	33.5	83.4	0.98	0.45	2.80	4.30	0.50	-1.30	-3.10	785.3	400.2	400.2	0.002	35.31	386.0	0.45	38.13	32.30	k
FRB20190109A	0	108.0	5.2	13.76	1.65	1.19	6.40	2.20	6.10	-8.10	800.2	400.2	583.0	0.100	38.97	440.0	1.50	41.28	32.63	k
FRB20190109A	1	108.0	5.2	13.76	3.40	1.19	6.40	2.20	4.60	-8.50	800.2	400.2	523.6	0.100	38.92	440.0	3.09	41.23	32.72	k
FRB20190109B	0	253.5	1.2	6.88	0.34	1.20	3.00	0.26	2.50	-65.00	492.4	400.2	408.1	0.009	36.40	93.1	0.34	39.00	31.46	both
FRB20190110A	0	65.0	47.4	2.95	0.20	1.54	3.80	0.38	6.30	-11.00	472.7	400.2	411.0	0.231	39.34	89.3	0.16	42.03	35.13	both
FRB20190110C	0	247.0	41.4	2.95	0.39	0.64	1.40	0.22	24.50	-186.00	477.7	400.2	427.4	0.112	38.27	86.2	0.35	40.98	34.06	both
FRB20190111A	0	217.0	26.8	5.90	0.36	3.60	17.00	0.54	6.35	-6.78	800.2	400.2	638.9	0.066	39.07	426.6	0.34	41.42	33.40	k
FRB20190111A	1	217.0	26.8	5.90	0.44	3.60	17.00	0.54	7.91	-23.30	649.7	400.2	474.4	0.066	38.94	266.1	0.41	41.29	33.66	both
FRB20190111A	2	217.0	26.8	5.90	0.79	3.60	17.00	0.54	-2.30	-5.80	635.8	400.2	400.2	0.066	38.87	251.2	0.74	41.22	33.81	both
FRB20190111B	0	260.0	13.5	3.93	0.16	0.32	0.78	0.20	1.90	-17.20	609.1	400.2	422.5	1.348	40.21	490.5	0.07	43.19	35.72	k
FRB20190112A	0	258.0	61.2	9.83	1.64	1.40	16.20	11.01	57.10	-51.40	800.2	564.6	697.7	0.348	40.56	317.5	1.22	42.63	33.95	both
FRB20190113A	0	108.1	-3.0	6.88	1.82	1.30	5.60	2.20	7.30	-2.80	800.2	491.9	800.2	0.190	39.62	366.9	1.53	42.06	33.56	both
FRB20190114A	0	8.9	19.2	4.92	1.34	0.55	2.30	0.38	11.10	-89.00	500.0	400.2	425.8	0.869	40.31	186.5	0.72	42.96	35.38	both
FRB20190116F	0	261.7	75.0	2.95	1.23	0.49	1.54	1.50	3.60	-3.80	800.2	400.2	637.5	0.214	39.07	485.7	1.01	41.65	34.18	k
FRB20190118A	0	253.3	11.6	1.97	0.14	9.30	18.00	0.28	19.42	-56.71	580.9	400.2	474.9	0.093	39.27	197.6	0.13	42.02	35.32	both
FRB20190122C	2	200.6	17.6	14.75																

Table 6 (*continued*)

FRB name	Sub num	RA(J2000) ($^{\circ}$)	DEC(J2000) ($^{\circ}$)	Δt_{bc} (ms)	Δt_{fitb} (ms)	S_{ν} (Jy)	F_{ν} (Jy · ms)	Δt_{sc} (ms)	γ	r	ν_{max} (MHz)	ν_{min} (MHz)	ν_{peak} (MHz)	z	$\log E$ (erg)	$\Delta\nu$ (MHz)	Δtrw (ms)	$\log L$ (erg/s)	$\log T_B$ (K)	Note
FRB20190131E	0	195.7	80.9	0.98	0.23	3.00	5.10	0.16	22.00	-63.10	576.8	400.2	476.5	0.174	39.27	207.3	0.20	42.11	35.99	both
FRB20190201B	0	118.2	55.6	2.95	0.80	0.81	2.30	0.57	1.80	-14.80	632.1	400.2	425.9	0.697	40.12	393.6	0.47	42.90	35.80	k
FRB20190201A	0	64.0	84.8	0.98	0.61	2.60	3.10	0.72	0.10	-0.20	800.2	400.2	476.6	0.103	38.59	441.4	0.55	41.56	35.46	k
FRB20190202A	0	344.2	17.1	1.97	0.71	41.00	95.00	0.72	5.13	-12.38	757.8	400.2	492.3	0.210	40.73	432.8	0.59	43.44	36.66	k
FRB20190203B	0	130.6	61.9	2.95	0.30	0.49	0.93	0.58	1.50	-8.50	735.7	400.2	437.5	0.520	39.48	510.1	0.20	42.38	35.30	k
FRB20190203A	0	133.7	70.8	3.93	0.55	1.21	4.00	0.83	25.00	-75.00	563.4	400.2	472.9	0.337	39.76	218.2	0.41	42.36	34.99	both
FRB20190204A	0	161.3	61.5	7.86	1.81	0.24	1.50	0.88	2.40	-28.00	557.9	400.2	418.2	0.382	39.39	217.9	1.31	41.73	33.90	both
FRB20190205A	0	342.2	83.4	2.95	0.60	0.74	1.70	0.69	18.30	-47.30	605.6	400.2	485.7	0.622	39.95	333.2	0.37	42.80	35.55	both
FRB20190206B	0	49.8	79.5	19.66	7.10	0.95	9.60	9.00	11.60	-24.60	687.6	400.2	506.4	0.219	39.78	350.3	5.82	41.86	33.04	k
FRB20190206A	0	244.8	9.4	5.90	0.80	1.40	9.10	2.74	38.00	-65.70	644.6	443.2	534.5	0.062	38.66	213.8	0.76	40.87	33.08	both
FRB20190208B	0	91.0	80.9	0.98	0.10	10.30	14.30	0.12	0.69	-8.02	713.9	400.2	417.9	0.651	40.85	518.0	0.06	43.92	37.82	k
FRB20190208C	0	141.6	83.6	0.98	0.41	1.27	1.74	0.45	18.70	-54.60	583.2	400.2	474.9	0.115	38.43	204.0	0.37	41.35	35.25	both
FRB20190210B	0	104.2	23.7	2.95	0.40	2.60	5.30	0.36	-2.45	-3.09	696.1	400.2	400.2	0.488	40.14	440.4	0.27	43.00	36.05	k
FRB20190210D	0	307.8	55.5	1.97	0.58	1.37	2.50	0.27	20.70	-24.40	800.2	449.9	611.8	0.151	38.95	403.2	0.50	41.75	34.70	k
FRB20190210E	0	313.6	86.7	1.97	0.96	0.69	1.45	1.10	13.40	-40.50	599.4	400.2	472.2	0.505	39.68	299.8	0.64	42.53	35.71	both
FRB20190211B	0	299.6	61.4	0.98	0.10	0.30	1.35	0.15	1.40	-7.50	764.9	400.2	440.1	0.099	38.16	400.9	0.09	40.55	34.56	k
FRB20190212B	0	140.0	52.1	2.95	0.23	1.55	3.70	0.50	-2.05	-3.60	702.0	400.2	400.2	0.546	40.08	466.5	0.15	42.89	35.92	k
FRB20190212D	0	178.8	66.7	21.63	1.05	0.42	5.70	15.90	-4.20	-0.30	681.6	400.2	400.2	1.156	40.92	606.6	0.49	43.12	34.28	k
FRB20190214C	0	218.9	19.4	6.88	1.68	1.02	5.20	1.08	4.90	-16.70	671.7	400.2	463.1	0.492	40.20	405.1	1.13	42.67	34.79	k
FRB20190215B	0	335.0	45.3	1.97	0.86	2.20	5.60	0.92	-1.27	-2.09	800.2	400.2	400.2	0.051	38.15	420.3	0.82	40.76	34.31	k
FRB20190218B	0	268.7	17.9	17.69	2.05	0.57	5.90	14.10	46.20	-60.00	715.2	483.4	588.0	0.442	40.26	334.2	1.42	42.41	33.41	both
FRB20190218C	0	157.0	78.0	0.98	0.21	19.00	31.00	0.11	3.08	-16.09	643.0	400.2	440.4	0.221	40.24	296.4	0.17	43.11	37.07	both
FRB20190220A	0	237.2	74.2	1.97	0.55	0.34	0.68	0.24	-3.30	-3.30	642.4	400.2	400.2	0.098	37.81	265.9	0.50	40.55	34.08	both
FRB20190221A	0	132.6	9.9	2.95	0.97	1.23	2.33	0.41	5.10	-23.90	606.5	400.2	444.8	0.092	38.34	225.4	0.89	41.10	34.14	both
FRB20190221B	0	286.8	27.9	6.88	3.94	0.69	5.60	4.90	-0.30	-2.40	800.2	400.2	400.2	0.163	39.18	465.2	3.39	41.34	33.75	k
FRB20190221D	0	24.8	60.9	1.97	0.77	0.65	1.13	0.95	0.30	-2.40	800.2	400.2	427.2	0.231	38.83	492.5	0.63	41.68	35.07	k
FRB20190222B	0	160.7	19.6	21.63	1.52	0.40	4.40	5.26	-1.80	-10.20	593.5	400.2	400.2	0.439	39.96	278.2	1.06	42.08	33.41	both
FRB20190222C	0	239.2	40.0	1.97	0.68	0.44	0.83	0.74	9.30	-53.90	536.4	400.2	436.3	0.473	39.34	200.7	0.46	42.24	35.52	both
FRB20190223A	0	64.7	87.7	3.93	0.76	0.47	1.58	0.87	21.80	-103.00	516.5	400.2	444.8	0.286	39.18	149.6	0.59	41.76	34.49	both
FRB20190224A	0	60.5	83.4	16.71	2.04	0.63	8.50	5.77	2.60	-60.00	497.5	400.2	408.9	0.762	40.75	171.4	1.16	42.86	34.30	both
FRB20190224E	0	183.0	61.5	1.97	0.55	2.03	4.00	0.57	2.22	-8.64	762.2	400.2	454.9	0.369	39.82	495.7	0.40	42.67	35.93	k
FRB20190226B	0	273.6	61.8	18.68	4.00	0.38	2.38	4.90	29.90	-39.30	745.3	459.4	585.2	0.570	40.10	448.9	2.55	42.49	33.42	k
FRB20190226C	0	17.5	26.8	4.92	1.31	0.39	1.41	1.50	6.60	-42.00	548.3	400.2	433.3	0.795	40.03	265.9	0.73	42.73	35.14	both
FRB20190227B	0	220.5	39.8	0.98	0.40	0.48	0.71	0.47	-0.50	-0.80	800.2	400.2	400.2	0.259	38.70	503.4	0.32	41.63	35.70	k
FRB20190228A	0	183.5	22.9	30.47	2.25	1.79	35.80	18.91	52.60	-51.90	800.2	538.4	664.7	0.365	40.93	357.3	1.65	42.76	33.16	both
FRB20190301B	0	69.5	74.1	3.93	1.32	0.40	0.85	1.60	-1.50	-13.40	575.5	400.2	400.2	0.523	39.41	267.0	0.87	42.26	35.05	both
FRB20190301D	0	278.7	74.7	5.90	0.36	0.39	1.50	0.54	3.60	-29.40	562.7	400.2	425.4	1.159	40.37	350.9	0.17	43.12	35.32	both
FRB20190303B	0	128.7	66.0	4.92	0.72	9.40	42.00	1.57	-1.68	-2.56	786.7	400.2	400.2	0.061	39.19	410.1	0.67	41.56	34.31	k
FRB20190303D	0	179.6	70.8	2.95	0.81	0.59	1.17	1.00	-0.90	-5.60	704.3	400.2	400.2	0.674	39.77	509.1	0.48	42.70	35.69	k
FRB20190304A	0	124.5	74.6	2.95	0.41	0.71	2.90	0.90	6.30	-67.30	504.7	400.2	419.4	0.405	39.73	146.8	0.29	42.27	35.28	both
FRB20190304B	0	204.9	24.2	2.95	0.33	0.67	2.22	0.62	-1.24	-7.40	646.5	400.2	400.2	0.420	39.63	349.8	0.23	42.26	35.32	k
FRB20190304C	0	223.0	26.7	2.95	0.95	0.53	1.32	1.10	22.30	-87.00	535.2	400.2	454.9	0.528	39.66	206.2	0.62	42.45	35.32	both
FRB20190308C	0	188.4	44.4	21.63	0.40	0.47	4.80	2.29	15.20	-61.00	550.7	400.2	453.4	0.454	40.09	218.9	0.28	42.24	33.40	both
FRB20190308C	1	188.4	44.4	21.63	0.55	0.47	4.80	2.29	13.90	-60.50	545.7	400.2	449.0	0.454	40.08	211.6	0.38	42.24	33.41	both
FRB20190308B	0	38.6	83.6	1.97	0.19	1.11	1.39	0.13	18.60	-52.90	587.9	400.2	477.2	0.015	36.57	190.6	0.18	39.48	32.82	both
FRB20190308B	1	38.6	83.6	1.97	0.52	1.11	1.39	0.13	9.50	-37.00	585.3	400.2	455.5	0.015	36.55	187.9	0.51	39.46	32.86	both
FRB20190309A	0	279.0	52.4	1.97	0.58	0.39	0.72	0.75	12.90	-64.00	535.8	400.2	442.9	0.248	38.71	169.2	0.47	41.54	34.88	both
FRB20190318A	0	324.1	74.5	12.78	0.93	1.55	14.20	6.23	0.04	-3.04	800.2	400.2	402.9	0.290	40.10	515.9	0.72	42.25	34.08	k
FRB20190320C	0	254.7	22.4	3.93	1.04	1.24	3.14	1.30	4.10	-2.20	800.2	400.2	442.0	0.275	39.44	510.2	0.82	42.14	34.88	k
FRB20190320E	0	76.6	89.2	2.95	0.83	4.40	12.30	0.72	6.06	-7.70	800.2	400.2	592.6	0.182	39.79	472.8	0.70	42.42	35.05	k
FRB20190322B	0	132.0	73.3	2.95	1.30	0.61	2.04	1.70	-0.10	-6.20	725.7	400.2	400.2	0.513	39.77	492.6	0.86	42.43	35.46	k
FRB20190323C	0	199.5	40																	

Table 6 (*continued*)

FRB name	Sub num	RA(J2000) ($^{\circ}$)	DEC(J2000) ($^{\circ}$)	Δt_{bc} (ms)	Δt_{fitb} (ms)	S_{ν} (Jy)	F_{ν} (Jy · ms)	Δt_{sc} (ms)	γ	r	ν_{max} (MHz)	ν_{min} (MHz)	ν_{peak} (MHz)	z	$\log E$ (erg)	$\Delta\nu$ (MHz)	Δtrw (ms)	$\log L$ (erg/s)	$\log T_B$ (K)	Note
FRB20190410A	0	263.5	-2.4	6.88	1.01	1.59	5.80	1.20	43.00	-85.00	607.9	437.4	515.7	0.073	38.59	182.9	0.94	41.06	33.18	both
FRB20190410B	0	265.8	15.2	1.97	0.42	0.22	0.45	0.21	18.70	-73.40	542.5	400.2	454.4	0.551	39.23	220.7	0.27	42.11	35.32	both
FRB20190411C	0	9.3	20.5	2.95	1.02	3.19	9.30	1.10	24.30	-26.10	800.2	473.1	636.5	0.122	39.35	367.2	0.91	41.93	34.49	both
FRB20190411C	1	9.3	20.5	2.95	0.89	3.19	9.30	1.10	11.70	-12.50	800.2	416.6	640.1	0.122	39.35	430.6	0.79	41.93	34.49	k
FRB20190412B	0	285.6	19.2	42.27	6.80	0.68	12.80	15.50	-4.00	-2.70	625.5	400.2	400.2	0.015	37.42	228.6	6.70	39.15	30.05	both
FRB20190414A	0	181.4	38.9	4.92	1.95	0.44	1.74	2.40	-3.40	-0.70	728.1	400.2	400.2	0.805	40.10	591.8	1.08	42.76	35.27	k
FRB20190415C	0	74.8	34.8	4.92	0.55	0.46	0.77	0.87	13.40	-32.00	648.9	400.2	495.3	0.459	39.34	362.9	0.38	42.28	34.61	k
FRB20190416B	0	172.2	36.0	5.90	0.79	0.69	1.47	0.49	-3.60	-23.50	511.9	400.2	400.2	0.541	39.67	172.1	0.51	42.53	34.96	both
FRB20190417C	0	45.7	71.3	0.98	0.41	7.90	10.80	0.43	24.78	-32.41	765.8	449.3	586.6	0.127	39.41	356.6	0.37	42.32	35.95	both
FRB20190418A	0	65.8	16.0	1.97	0.71	0.99	2.20	0.78	-4.80	-3.70	579.7	400.2	400.2	0.019	36.89	183.0	0.69	39.55	33.11	both
FRB20190419A	0	105.0	64.9	3.93	1.85	0.41	0.77	2.40	1.00	-29.00	538.6	400.2	407.1	0.341	38.99	185.5	1.38	41.84	34.66	both
FRB20190419B	0	255.3	86.7	1.97	0.66	4.60	7.90	0.25	5.65	-14.30	728.4	400.2	487.6	0.017	37.43	333.8	0.64	40.20	33.51	k
FRB20190420A	0	106.5	56.0	1.97	0.77	0.88	3.11	2.64	11.50	-6.10	800.2	528.7	800.2	0.528	40.28	414.9	0.50	42.92	35.40	both
FRB20190420C	0	248.1	37.2	13.76	1.95	0.44	4.13	8.00	-0.50	-6.40	700.0	400.2	400.2	0.585	40.19	475.2	1.23	42.42	34.10	k
FRB20190421B	0	82.5	62.3	2.95	1.12	5.10	16.40	1.20	-0.13	-0.80	800.2	400.2	400.2	0.245	40.01	498.0	0.90	42.60	35.72	k
FRB20190422A	0	48.6	35.1	29.49	3.22	0.60	9.10	2.70	42.00	-46.90	781.4	501.7	626.1	0.335	40.23	373.4	2.41	42.18	32.68	both
FRB20190422A	1	48.6	35.1	29.49	2.31	0.60	9.10	2.70	54.20	-63.70	740.5	506.3	612.3	0.335	40.22	312.6	1.73	42.17	32.70	both
FRB20190422A	2	48.6	35.1	29.49	2.00	0.60	9.10	2.70	24.00	-32.00	763.7	444.8	582.8	0.335	40.20	425.7	1.50	42.14	32.75	k
FRB20190423A	0	179.7	55.2	5.90	0.41	10.80	55.40	0.54	11.19	-30.52	632.6	400.2	480.7	0.143	40.14	265.5	0.36	42.48	34.80	both
FRB20190423A	1	179.7	55.2	5.90	2.37	10.80	55.40	0.54	-3.66	-5.59	593.0	400.2	400.2	0.143	40.06	220.3	2.07	42.40	34.96	both
FRB20190423B	0	298.6	26.2	9.83	2.49	0.87	7.00	3.00	62.40	-106.00	623.1	463.8	537.6	0.003	35.93	159.8	2.48	38.03	29.81	both
FRB20190423B	1	298.6	26.2	9.83	8.50	0.87	7.00	3.00	63.00	-116.00	604.1	455.6	524.6	0.003	35.92	149.0	8.47	38.02	29.83	both
FRB20190423C	0	349.1	87.0	7.86	0.16	1.23	4.37	2.48	1.90	-12.30	668.0	400.2	433.0	0.808	40.54	484.3	0.09	43.24	35.25	k
FRB20190425A	0	255.7	21.5	0.98	0.38	18.60	31.60	0.38	8.26	-10.56	800.2	400.2	591.8	0.002	36.35	400.9	0.38	39.12	32.78	k
FRB20190425B	0	210.1	88.6	1.97	1.11	1.25	3.10	1.30	22.40	-65.60	572.6	400.2	474.8	1.014	40.62	347.2	0.55	43.53	36.57	both
FRB20190426A	0	115.0	59.1	1.97	0.40	1.59	2.01	0.43	27.00	-71.70	577.8	403.7	483.0	0.232	39.13	214.5	0.32	42.12	35.35	both
FRB20190427A	0	78.9	7.8	1.97	0.34	3.90	9.50	0.65	-2.62	3.30	800.2	400.2	400.2	0.333	40.05	533.0	0.25	42.79	36.23	k
FRB20190428A	0	170.7	23.3	3.93	0.37	2.22	7.40	3.63	54.00	-48.80	800.2	560.1	696.0	0.973	41.13	473.7	0.19	43.90	35.85	both
FRB20190429B	0	329.9	4.0	16.71	6.38	0.74	5.00	7.80	99.00	-91.00	444.1	401.7	422.4	0.194	39.31	50.6	5.34	41.56	33.12	both
FRB20190430A	0	77.7	87.0	19.66	3.38	0.75	7.70	3.23	4.70	-29.10	574.6	400.2	433.8	0.228	39.65	214.1	2.75	41.73	33.11	both
FRB20190430C	0	277.2	24.9	2.95	0.89	2.17	5.10	1.10	48.70	-48.80	800.2	530.6	659.3	0.252	39.75	337.5	0.71	42.47	34.94	both
FRB20190501B	0	261.4	54.4	5.90	0.93	0.88	3.20	1.10	-0.03	-6.80	714.8	400.2	400.2	0.748	40.30	549.8	0.53	42.98	35.35	k
FRB20190502C	0	155.6	83.0	1.97	0.53	3.60	8.30	0.32	9.00	-26.80	634.3	400.2	473.2	0.308	39.99	306.2	0.40	42.75	35.98	both
FRB20190515B	0	0.8	3.4	4.92	0.38	2.80	11.30	1.88	0.77	-9.30	685.6	400.2	417.0	0.802	40.93	514.4	0.21	43.58	36.04	k
FRB20190515D	0	67.1	-5.0	4.92	0.42	3.00	8.80	1.49	30.60	-54.30	651.5	431.6	530.2	0.341	40.16	294.9	0.31	42.82	35.10	both
FRB20190516B	0	167.3	7.4	13.76	1.49	1.13	9.90	3.72	1.10	-12.20	647.1	400.2	419.4	1.267	41.26	559.8	0.66	43.67	35.14	k
FRB20190517C	0	87.5	26.6	1.97	0.38	3.10	8.70	0.15	8.48	-50.20	539.4	400.2	435.5	0.063	38.56	147.9	0.35	41.14	34.57	both
FRB20190518C	0	242.0	4.6	2.95	0.64	6.70	14.80	0.29	6.39	-15.10	730.2	400.2	494.3	0.369	40.43	451.7	0.46	42.32	36.02	k
FRB20190518D	0	174.7	89.3	1.97	0.26	1.36	3.00	0.39	5.40	-15.60	698.5	400.2	475.6	0.064	38.15	317.3	0.24	40.84	34.15	k
FRB20190518G	0	94.8	75.5	0.98	0.67	0.99	1.76	0.72	19.80	-75.30	543.6	400.2	456.4	0.437	39.62	206.0	0.46	42.53	36.37	both
FRB20190519E	0	168.3	41.6	0.98	0.41	1.00	1.46	0.45	2.00	4.10	800.2	551.0	800.2	0.665	40.16	415.0	0.25	43.21	36.26	both
FRB20190519F	0	165.6	77.2	6.88	1.36	0.75	4.00	1.36	21.70	-86.40	534.4	400.2	453.9	0.765	40.47	236.8	0.77	42.99	35.06	both
FRB20190519H	0	343.0	87.4	2.95	0.25	3.20	6.60	0.31	2.33	-14.00	652.9	400.2	435.0	1.164	41.03	546.8	0.12	44.05	36.82	k
FRB20190519J	0	296.2	86.9	1.97	0.46	0.63	1.70	0.50	24.30	-25.90	461.0	400.2	419.5	0.577	39.82	95.9	0.29	42.58	35.89	both
FRB20190520A	0	273.5	26.3	1.97	0.65	1.08	2.40	0.71	11.40	-54.30	546.0	400.2	444.4	0.312	39.44	191.3	0.49	42.21	35.52	both
FRB20190527A	0	12.4	8.0	57.02	2.67	0.47	10.10	5.08	47.00	-122.00	556.1	422.4	484.7	0.537	40.59	205.5	1.74	42.44	32.65	both
FRB20190527A	1	12.4	8.0	57.02	2.47	0.47	10.10	5.08	30.70	-133.00	512.2	400.2	449.1	0.537	40.55	172.1	1.61	42.41	32.72	both
FRB20190529A	0	68.1	40.3	3.93	1.04	0.47	1.45	1.50	24.20	-97.00	528.9	400.2	453.4	0.523	39.69	196.1	0.68	42.39	35.01	both
FRB20190530A	0	68.7	60.6	1.97	1.02	0.58	1.69	1.30	17.70	-91.00	517.3	400.2	441.1	0.385	39.47	162.1	0.74	42.15	35.45	both
FRB20190531C	0	331.1	43.0	2.95	1.45	0.37	1.20	1.90	18.30	-74.00	540.6	400.2	453.0	0.304	39.12	183.0	1.11	41.73	34.67	both
FRB20190531E	0	15.2	0.5	0.98	0.47	2.70	5.30	0.56	1.10	4.60	800.2	527.0	800.2	0.245	39.82	340.2	0.37	42.63	35.80	both
FRB20190601B	0	1																		

Table 6 (*continued*)

FRB name	Sub num	RA(J2000) ($^{\circ}$)	DEC(J2000) ($^{\circ}$)	Δt_{bc} (ms)	Δt_{fitb} (ms)	S_{ν} (Jy)	F_{ν} (Jy · ms)	Δt_{sc} (ms)	γ	r	ν_{max} (MHz)	ν_{min} (MHz)	ν_{peak} (MHz)	z	$\log E$ (erg)	$\Delta\nu$ (MHz)	Δtrw (ms)	$\log L$ (erg/s)	$\log T_B$ (K)	Note
FRB20190616A	0	234.0	34.5	1.97	0.65	0.73	1.67	0.79	-0.80	-1.80	800.2	400.2	400.2	0.113	38.33	445.1	0.59	41.01	34.54	k
FRB20190617A	0	178.6	83.9	4.92	1.49	5.80	21.00	1.50	0.45	-9.35	673.2	400.2	409.9	0.065	38.94	290.6	1.40	41.41	34.13	both
FRB20190617B	0	56.4	1.2	13.76	7.58	0.99	9.20	9.50	10.60	-38.40	586.7	400.2	459.3	0.166	39.47	217.4	6.50	41.57	33.20	both
FRB20190618A	0	321.2	25.4	1.97	0.55	2.40	4.30	0.58	3.34	-35.80	540.4	400.2	419.3	0.068	38.31	149.7	0.51	41.08	34.56	both
FRB20190619B	0	231.7	82.2	0.98	0.52	1.96	4.50	0.59	-0.50	-5.60	731.8	400.2	400.2	0.159	39.06	384.5	0.45	41.77	35.88	k
FRB20190619D	0	114.8	41.6	32.44	1.39	0.48	6.50	12.00	-6.46	4.90	800.2	400.2	400.2	0.267	39.69	506.8	1.10	41.66	32.69	k
FRB20190621B	0	193.1	55.6	1.97	1.38	0.30	1.19	1.80	-0.50	-7.70	670.9	400.2	400.2	1.072	40.18	560.9	0.67	42.90	36.15	k
FRB20190621C	0	206.6	5.2	0.98	0.44	1.98	2.38	0.51	39.10	-101.00	564.4	417.5	485.4	0.530	39.95	224.7	0.29	43.05	36.79	both
FRB20190621D	0	270.6	78.9	3.93	2.29	0.89	4.30	2.60	7.40	-22.30	651.1	400.2	472.1	0.588	40.29	398.4	1.44	42.80	35.36	k
FRB20190622A	0	299.0	85.8	1.97	1.19	0.61	1.28	1.40	0.90	-15.60	605.0	400.2	411.9	1.112	40.25	432.6	0.56	43.26	36.46	k
FRB20190624A	0	168.3	69.8	5.90	1.52	0.58	3.01	0.95	-5.30	2.20	704.0	400.2	400.2	0.966	40.49	597.2	0.77	43.07	35.39	k
FRB20190624B	0	304.6	73.6	0.98	0.37	16.50	20.00	0.40	34.80	-43.20	754.3	475.4	598.8	0.058	39.00	295.2	0.35	41.94	35.56	both
FRB20190625A	0	227.9	32.9	58.00	3.92	0.35	11.90	16.90	-1.10	-8.10	639.7	400.2	400.2	0.225	39.80	293.4	3.20	41.35	31.89	both
FRB20190625C	0	73.2	11.1	0.98	0.55	2.22	4.02	0.63	0.30	-5.90	768.7	400.2	410.7	0.327	39.67	489.1	0.41	42.54	36.55	k
FRB20190625D	0	115.0	4.9	1.97	0.69	5.30	12.10	0.72	17.84	-76.10	535.5	400.2	450.0	0.610	40.75	217.8	0.43	43.60	36.80	both
FRB20190627A	0	195.9	0.8	1.97	0.66	1.98	2.62	0.80	9.30	-27.30	634.6	400.2	474.6	0.336	39.57	313.2	0.50	42.58	35.80	both
FRB20190628B	0	248.5	80.1	2.95	0.27	0.75	1.39	0.47	-6.00	-0.40	583.5	400.2	400.2	0.322	39.18	242.3	0.20	42.04	35.13	both
FRB20190629A	0	6.3	12.7	3.93	1.14	0.82	3.05	1.70	24.70	-35.30	733.6	440.1	568.2	0.444	39.97	423.9	0.79	42.56	34.91	k
FRB20190630D	0	143.4	8.9	1.97	0.56	1.73	2.60	0.63	-2.30	-1.60	780.6	400.2	400.2	0.226	39.14	466.3	0.45	42.05	35.53	k
FRB20190701C	0	96.4	81.6	1.97	1.44	0.88	2.50	1.80	46.20	-211.00	495.5	402.2	446.4	0.943	40.44	181.3	0.74	43.27	36.41	both
FRB20190701D	0	112.1	66.7	8.85	1.40	1.33	8.60	1.53	6.49	-20.90	651.8	400.2	467.6	0.900	40.96	478.1	0.74	43.42	35.21	k
FRB20190609C	0	73.3	24.1	3.93	2.07	0.64	1.91	4.10	15.20	-138.00	481.3	400.2	422.9	0.328	39.36	61.1	1.56	42.01	35.34	both
FRB20190226B	0	273.6	61.7	10.81	4.00	0.38	2.38	8.00	29.90	-39.30	706.4	474.3	578.8	0.570	40.09	147.8	2.55	42.49	34.77	both
FRB20190430C	0	277.2	24.8	2.95	0.89	5.80	15.20	1.80	48.70	-48.80	800.2	527.8	655.2	0.251	40.21	217.7	0.71	42.89	36.41	both
FRB20190110C	0	249.3	41.4	2.95	0.75	0.64	1.40	1.50	28.20	-202.00	477.7	400.2	427.4	0.110	38.26	69.8	0.68	40.96	35.24	both
FRB20190113A	0	108.3	-3.0	6.88	1.82	1.10	5.70	3.60	7.30	-2.80	800.2	491.9	800.2	0.191	39.63	258.8	1.53	41.99	34.65	both
FRB20180910A	0	354.8	89.0	0.98	0.21	6.50	5.60	0.24	0.05	-0.53	800.2	400.2	417.6	0.623	40.40	246.4	0.13	43.67	38.94	k
FRB20190303D	0	185.3	70.7	2.95	0.81	0.59	1.17	1.60	-0.90	-5.60	564.8	400.2	440.8	0.674	39.81	98.3	0.48	42.74	36.73	both
FRB20190328C	0	75.6	82.1	3.93	0.77	4.70	14.90	2.30	0.70	-2.70	800.2	400.2	459.0	0.376	40.41	290.6	0.56	43.05	37.12	k
FRB20190107B	0	49.3	83.4	0.98	0.45	2.80	4.30	0.90	-1.30	-3.10	784.4	400.2	400.2	0.002	35.31	383.3	0.45	38.13	32.98	k
FRB20190210C	0	313.9	89.2	1.97	0.29	2.37	3.60	0.25	0.35	-1.50	800.2	400.2	448.5	0.580	40.17	253.2	0.18	43.19	38.09	k
FRB20190127B	0	169.3	83.5	67.83	2.50	0.63	11.40	42.80	5.30	-7.70	800.2	400.2	562.2	0.609	40.82	248.6	1.55	42.77	35.48	both
FRB20180909A	0	120.0	57.0	15.73	6.31	0.43	0.90	13.00	-0.30	-1.30	800.2	400.2	400.2	0.316	38.98	304.0	4.80	41.78	34.21	k
FRB20190201A	0	95.9	83.8	0.98	0.61	2.60	3.10	1.20	0.10	-0.20	789.0	400.2	464.9	0.109	38.63	350.5	0.55	41.60	35.95	k
FRB20190308B	0	49.3	83.4	1.97	0.19	1.11	1.39	0.13	18.60	-52.90	587.9	400.2	477.2	0.016	36.63	184.7	0.18	39.54	34.92	both
FRB20190308B	1	49.3	83.4	1.97	0.52	1.11	1.39	0.13	9.50	-37.00	585.3	400.2	455.5	0.016	36.61	182.1	0.51	39.52	34.07	both